Osteosarcoma tumors maintain intra-tumoral heterogeneity, even while adapting to environmental pressures that drive clonal selection

Sanjana Rajan[1,2], Camille A. McAloney[2,3], Tatyana A. Vetter[4], Maren Cam[2], Amy C. Gross[2], Cenny Taslim[2], Meng Wang[2], Matthew V. Cannon[2], Alexander Oles[5], Emily Franz[1,2], Kevin M. Flanigan[4,6], Ryan D. Roberts[2,6,7*]

INSTITUTIONS:

[1]Molecular, Cellular, and Developmental Biology Program, The Ohio State University, Columbus, Ohio, USA

[2]Center for Childhood Cancers and Blood Diseases, Abigail Wexner Research Institute at Nationwide Children's Hospital, Ohio, USA

[3]Department of Veterinary Biosciences, College of Veterinary Medicine, The Ohio State University, Columbus, Ohio, USA

[4]Center for Gene Therapy, Abigail Wexner Research Institute, Nationwide Children's Hospital, Columbus, Ohio, USA

[5]Department of Biochemistry & Molecular Biology, Medical University of South Carolina, Charleston, South Carolina, USA

[6]Division of Pediatric Hematology, Oncology, and BMT, Nationwide Children's Hospital, Columbus, Ohio, USA

[7]The Ohio State University James Comprehensive Cancer Center, Columbus, Ohio, USA

*Corresponding author

Correspondence:

Ryan D. Roberts
Division of Pediatric Hematology, Oncology, and BMT
Nationwide Children's Hospital
700 Children's Drive, Columbus, OH 43205
Email: Ryan.Roberts@nationwidechildrens.org
Phone: 614-722-29966; Fax: 614-355-2927

Abstract

Background

Tumors are complex tissues containing collections of phenotypically diverse malignant and non-malignant cells. We know little of the mechanisms that govern heterogeneity within tumor cells themselves and the role it plays in overcoming stresses, such as adaptation to a metastatic microenvironment. Osteosarcoma is an ideal model for studying these mechanisms—it exhibits widespread inter- and intra-tumoral heterogeneity, progresses with predictable patterns of metastasis, and lacks clear targetable driver mutations. Understanding the processes that facilitate adaptation to primary and metastatic microenvironments could inform the development of therapeutic strategies with potential to significantly impact clinical outcomes.

Results

We investigated single-cell RNA-sequencing profiles of 47,977 cells obtained from cell line and patient-derived xenograft models as osteosarcoma cells adapted to different environments. Tumor cells from almost all models maintained phenotypic heterogeneity as they adapted to the selective pressures imposed during bone and lung colonization. Subsets of cells identified within primary bone and metastatic lung tumors retained unique transcriptional phenotypes associated with distinct pathways, including heterogeneity in glucose metabolism that we validated using immunofluorescence staining. Finally, by leveraging concurrent lineage tracing and single-cell

transcriptomics, we found that lung colonization enriches for clonal populations with diverse phenotypes, each of which conserves phenotype across cellular generations.

Conclusions

Adaptation to environmental stressors occurs through complex and dynamic phenotypic adaptations, although heterogeneity is maintained, even in conditions that enforce clonal selection. These findings likely reflect a retention of developmental processes that promote the robustness of a tumor cell population in the face of selective pressures.

Key words

Osteosarcoma, heterogeneity, phenotype, clonal selection, microenvironment, metastasis

Background

Osteosarcoma is the most common malignant tumor of bone in pediatric patients(1). This aggressive disease occurs in the metaphyseal region of the long bones, coinciding with the anatomical location of bone growth(2). Localized disease has a favorable five-year survival rate of over 70%(3) that plummets to lower than 20% in the event of metastasis(4). Unfortunately, survival rates for patients with metastases have not changed since the introduction of chemotherapy in the 1980s(5). Indeed, patients are staged solely based on the presence or absence of metastasis(6). One unique feature of osteosarcoma is its extreme tropism for the lung: less than 2% of patients develop lesions in other organs(7,8). Transcriptional profiles adopted by individual tumor cells as they colonize bone and lung tissues remain poorly studied in this disease. While others have reported that osteosarcoma metastasis is a polyclonal process(9), the molecular pathways enriched in these clonal subsets during tissue colonization remain to be studied at a single-cell level and could provide novel insights into tumor vulnerabilities that might be missed using bulk methods.

Since most osteosarcoma patients have disseminated tumor cells at the time of diagnosis(6,10), we have focused on the selective pressures of lung colonization rather than the early steps of metastasis that result in dissemination(11–15). On exposure to the lung colonization bottleneck, a large percentage of cells die such that only the fittest cells can pass(14). Whether this fitness comes from rare but pre-existing clones that exhibit an inherent survival advantage or from an active adaptation response remains unknown. This is a fundamental question that has largely remained unanswered due to technical limitations. In this study, we overcome this by combining single-cell transcriptomics with lineage tracing to study both clonal evolution and transcriptional adaptation simultaneously and cell-by-cell.

In this study, we analyzed single cell transcriptomic libraries of 47,977 osteosarcoma cells obtained from cell lines and patient-derived xenograft (PDX) models, grown as orthotopic primary and metastatic tumors to study the role of intra-tumor phenotypic heterogeneity in tibia and lung colonization. We identified that osteosarcoma cells maintained phenotypic heterogeneity despite adapting their transcriptional phenotypes to tibia and lung microenvironmental conditions. This phenotypic heterogeneity was marked by the existence of tumor subsets displaying heterogeneous activation of distinct pathways, including glycolysis. Using immunofluorescence we validated heterogeneity in glycolysis activity in both primary and metastatic tumors. Furthermore, we validated the heterogeneous activation of multiple pathways identified in our preclinical models using publicly available single cell RNA sequenced primary patient tumor datasets. Finally, we combined a lentivirus-based lineage tracing system with single cell transcriptomics to study phenotype and clonal dynamics simultaneously during tissue colonization. Based on these investigations, we identified that osteosarcoma cells undergo dynamic changes in their transcriptional phenotype as they adapt to different microenvironmental conditions, while simultaneously maintaining an overall degree of transcriptional heterogeneity in

the wake of clonal selection. Overall, these data highlight the importance of understanding intra-tumor heterogeneity in the context of tumor cell adaptations during tissue colonization.

Results

Transcriptional heterogeneity in cell line and PDX models of osteosarcoma

Recent work has shown that osteosarcoma tumors collected directly from patients exhibit significant transcriptional heterogeneity(16,17). However, it is unclear if this heterogeneity is maintained within cell line and PDX models of disease(6). We investigated phenotypic heterogeneity within two *in vitro* and *in vivo* models of osteosarcoma by performing single-cell RNA sequencing (scRNA-seq). We generated transcriptomic libraries from a cell line (OS-17) and a PDX (NCH-OS-7; refer to supplementary ***Table S 1*** for full characteristics as per PDX-MI standards) grown in cell culture or as subcutaneous flank tumors (>2,500 cells per model). To distinguish tumor cells from murine host cells, we separated cells with reads that mapped to the human genome from those that mapped to mouse. Principal component analysis identified that majority of the variation in gene expression of tumor cells was dominated by cell cycle related genes, a common finding in proliferative malignant tissues(18) (supplementary ***Figure S 1***). Scaling out cell-cycle related genes unmasked underlying heterogeneity that did not correspond to variation arising solely from cells being in different states of cell cycle (supplementary ***Figure S 1***, ***Figure 1***Figure 1A, B). Using genes that were differentially upregulated in each cluster relative to the remaining cells in each sample, we identified pathways enriched in these subsets of cells (***Figure 1***C). While subsets within each model shared some enriched gene sets--for example, OS-17 cells in cluster 0 and cluster 1 showed enrichment for epithelial to mesenchymal transition (EMT) genes--none of the subsets had completely identical profiles, suggesting that these subsets are indeed functionally distinct. Interestingly, while EMT transcription factors play an important role in promotion of osteosarcoma cell invasion and metastasis(19), expression of EMT-related genes was associated with certain, distinct subsets. Furthermore, individual subsets had

differentially expressed genes that were associated with multiple gene sets. For example, OS-17 cells in cluster 2 were enriched for E2F targets, G2M checkpoint target genes, and MYC target genes; while NCH-OS-7 cells in cluster 0 were enriched for genes associated with EMT, glycolysis, hypoxia, and MYC target genes. This identification of gene sets exclusive to specific clusters of cells validated that these cell line and PDX models demonstrate intra-tumor phenotypic heterogeneity.

Transcriptional signatures associated with colonization of bone and lung microenvironments

Microenvironment cues play a critical role in shaping transcriptional plasticity(20). We hypothesized that transcriptional signatures shared across models upon adaptation to tibia or lung microenvironments will inform characteristics that are microenvironment-specific rather than tumor-specific. Single cell suspensions of two cell lines and two PDXs were injected intra-tibially or intra-venously to generate orthotopic models of primary and metastatic lesions (***Figure 2***A schematic). Spontaneous metastases from orthotopic primary tumors could not be investigated since mice bearing orthotopic lesions reached humane endpoint criteria before lung metastases were detected. Both the PDXs included in this study (NCH-OS-2, NCH-OS-7) are early passage (passage 3, passage 5) and were obtained from patient lung metastases to study the phenotypic profiles of cells that have survived the metastatic bottleneck.

***Table 1*. Characteristics of osteosarcoma models used in this study**

Model	Species	Type	Host	Endpoint	Characteristics
OS-17	Human	Cell Line	Icr-scid	70 days	Low passage, very well-characterized, reliable metastases
143B	Human	Cell Line	Icr-scid	65 days	Widely utilized, very well-characterized, reliable metastases
NCH-OS-2	Human	PDX	Icr-scid	200 days	Very low-passage, highly penetrant, from an untreated synchronous metastasis

NCH-OS-7	Human	PDX	Icr-scid	184 days	Very low-passage, highly penetrant, from a heavily-pretreated, multiply-relapsed metastasis

To study the transcriptional profiles associated with tibia and lung colonization, we performed a pseudo-bulk analysis of the scRNA-seq data and identified genes differentially expressed in primary tumors or metastatic lesions relative to their corresponding starting population (cell culture/flank tumors). The majority of the differentially regulated genes were unique to each model, with only 0.3-0.8% of genes shared across all four models (***Figure 2***B). Using genes that were either up- or down-regulated in at least three of the four models (2.7-5.6% of genes), we performed pathway enrichment analysis to identify pathways associated with colonization of tibia or lung tissues (***Figure 2***C). Genes that were significantly upregulated upon tibia colonization included those associated with glycolysis, hypoxia, MYC targets, fatty acid metabolism, and oxidative phosphorylation. None of the identified downregulated gene sets were statistically significant. Gene sets that were most significantly upregulated with lung colonization included those associated with TNFα signaling via NFκB and EMT, whereas those most significantly downregulated included MYC targets and MTORC1 signaling. Overall, we identified common pathways that were differentially regulated across the four models upon tibia and lung colonization.

Transcriptional heterogeneity of individual cells within a tumor

We analyzed single cell transcriptional profiles of the above datasets using our scRNA-seq bioinformatics workflow to study the role of intra-tumor heterogeneity in tissue colonization (***Figure 3***A). To estimate the degree of intra-tumor heterogeneity in our models, we computed intra-tumor heterogeneity scores (ITH scores) from the average Euclidian distance between each cell and every other cell in the same dataset(18). Since osteosarcoma can arise from transformed progenitor cells with osteoblastic differentiation and osteoid production(6), we compared the heterogeneity scores in osteosarcoma cells relative to human primary osteoblast cells grown in

cell culture. We found that irrespective of growth environment conditions, osteosarcoma cells had significantly higher ITH scores than normal osteoblast cells ($p < 0.001$, ***Figure 3***B). Upon investigation of the transcriptional profiles of osteoblast cells, we found that they exhibit a moderate level of heterogeneity, concurrent with previous reports(21) (supplementary ***Figure S 2***). We hypothesized that changes in microenvironment conditions would exert a selective pressure on osteosarcoma cells and cause a narrowing of transcriptional heterogeneity. Surprisingly, we found that osteosarcoma cells grown in tibia and lung microenvironments had significantly higher ITH scores compared to those grown *in vitro* or as flank tumors, with NCH-OS-7 being the only exception ($p < 0.001$, ***Figure 3***B). NCH-OS-7 cells showed no significant change of ITH scores in primary tumors relative to flank tumors but a significant decrease in ITH scores in metastatic lesions relative to flank tumor. Although, these cells were still more heterogeneous than the osteoblast sample. Overall, these results show that osteosarcoma cells are more transcriptionally heterogeneous than non-malignant osteoblast cells, and that osteosarcoma cells demonstrated an increase rather than a narrowing of transcriptional heterogeneity as they colonize the tibia and lung microenvironment.

To determine if primary tumors and metastatic lesions adopt similar phenotypes, we attempted to use an integrative approach across models (supplementary ***Figure S 3***). However, cells predominantly clustered by tumor model of origin, a phenomenon reported in other cancers including small cell lung cancers(18). This indicates a high degree of inter-tumor heterogeneity, a well-known characteristic of osteosarcoma tumors(22). We then compared primary and metastatic lesions within the same model (supplementary ***Figure S 4***). Using a cluster distribution analysis, we calculated the relative percentages of cells in each cluster to compare cells that colonized the tibia or the lung (supplementary ***Table*** S 2). While we identified that there was a significant overlap in the transcriptional profiles of cells that colonized the two microenvironments, certain cells adopted profiles specific to each microenvironment (***Figure 3***C). For instance, both

primary and metastatic OS-17 lesions had cells that adopted the phenotype associated with cluster 0 (47% in tibia and 42% in lung), however, cells with the phenotype associated with cluster 2 were significantly enriched in metastatic lesions (1% in tibia and 40% in lung). Using the pathway enrichment analysis outlined in Figure 1, we investigated the transcriptional profiles associated with each cluster (***Figure 3***D). While we were unable to use an integrative approach to study shared phenotypes across models due to the high inter-tumor heterogeneity, this approach allowed us to compare intra-tumor heterogeneity profiles within models. Pathways enriched in each cluster were unique, with high heterogeneity in activation of individual pathways across clusters within the same tumor. For example, while OS-17 cells in cluster 0 and cluster 3 were associated with MTORC1 signaling, only cells in cluster 3 were enriched for Glycolysis related genes. Using publicly available scRNA-seq datasets of patient primary tumors, we validated the heterogeneity in these transcriptional modules within individual tumor cells (supplementary ***Figure S 5*** - ***Figure S 8***). We therefore showed heterogeneity in activation of distinct pathways within tumor subsets, including those associated with glycolysis. This suggests osteosarcoma tumors are metabolically heterogeneous.

Metabolic heterogeneity in osteosarcoma tumors

To validate metabolic heterogeneity within individual tumors at the protein level, we performed immunofluorescence staining for a known activation marker of glycolysis, glucose transporter 1 (GLUT1), in lung metastases from two models (OS-17 and 143B). Sections were co-stained for vimentin to distinguish osteosarcoma cells from lung parenchyma. We observed variable staining for GLUT1 within individual metastatic lesions, suggesting that the observed heterogeneity was not a result of homogenous, spatially isolated lesions that stained differently from one another but instead was a result of heterogeneity intrinsic to individual lesions (***Figure 4***A, B). This observation was independent of the size of the lesions, suggesting that this metabolic heterogeneity is maintained over metastatic tumor growth. To confirm that this observation was

not as a result of stochastic gene expression changes in GLUT1 expression, we stained for other markers of glycolysis (hexokinase 2–HK2, carbonic anhydrase 9–CA9, monocarboxylate transporter 4–MCT4)(23) and a known upstream regulator of glycolysis, MYC(24). We measured the intensity of GLUT1 fluorescence of individual pixels, along with fluorescence of other markers, within areas positive for vimentin. We noted a high correlation in staining for GLUT1 and the other markers within 143B and OS-17 metastatic lesions (***Figure 4***C, supplementary ***Figure S 10***A). Immunofluorescence staining for markers of glycolysis in primary tumors from these models identified the same trend (supplementary ***Figure S* 9**, ***Figure S 10***B, C). This staining validated our bioinformatics finding of heterogeneity in glycolysis activation at the protein level and confirmed that this heterogeneity was not the result of stochastic gene expression changes.

Lung colonization bottleneck enriches for clones that adopt a growth-associated phenotype

We combined a lentivirus-based lineage tracing system with single cell transcriptomics to study phenotype and clonal dynamics simultaneously as osteosarcoma cells colonize tibia and lung microenvironments (***Figure 5***A). Lentivirus infection introduced a high diversity, heritable and polyA-tail capture compatible lineage tag library in osteosarcoma cells in cell culture. Sampling from this starting population of uniquely tagged cells, we generated orthotopic primary and metastatic lesions. Single cell libraries of primary tumors, metastatic tumors and cells in culture were processed bioinformatically to overlay phenotype and lineage information for each cell. At the level of phenotype, we noted that cells in tibia and lung cluster away from cells in cell culture, confirming our previous finding of adaptive changes as cells move from cell culture to tibia or lung microenvironments (***Figure 5***B). Since the lineage tags are passed on from one generation to the next as each cell divides, we used a frequency distribution analysis for lineage tags in the primary and metastatic tumors to determine if tibia or lung colonization were associated with an enrichment for clonal populations. In this context, “clonality” refers to cells with the same lineage

tag that originated from the same common ancestor. Lineage tag enrichment analysis for cells in cell culture identified 85% of cells to have a unique lineage tag, confirming that our starting population received lineage tags at high diversity. Surprisingly, cells from orthotopic primary tumors exhibited very little evidence of clonal selection, suggesting that most clones that were injected intra-tibially survived and colonized the tibia (***Figure 5***C). In contrast, cells from metastatic lesions demonstrated enrichment for distinct lineage tagged populations, suggesting selective enrichment for specific clonal families as cells traversed the lung colonization bottleneck (***Figure 5***C). We confirmed this pattern of clonal selection was reproducible in two independent replicates (supplementary ***Figure S 11***A; supplementary ***Table S 4***, ***Table*** S 5 for lentivirus distribution in cell culture). Interestingly, OS-17 cells from distinct, biological replicates grown *in vitro* or as metastatic lesions overlaid completely, suggesting that intra-tumor transcriptional heterogeneity of these osteosarcoma cells is not driven by individual tumor identity (supplementary ***Figure S 11***B).

We overlaid lineage information on phenotypic profiles to determine if these enriched clonal families in the lung adopted a common transcriptional profile. Interestingly, we found that cells within a given enriched clonal families clustered together, suggesting that cells that belonged to the same enriched clonal family passed on information regarding transcriptional phenotype from one generation to the next (***Figure 5***D). Pathway enrichment analysis for the genes differentially upregulated in the top 10 enriched clonal populations identified that these cells had genes associated with hypoxia, glycolysis, EMT and MTORC1 signaling (***Figure 5***E-F*,*

Table S 3 for differentially upregulated genes). Together, these results show that the adaptive transcriptional changes associated with lung colonization results in selection for clonal families that adopt a unique growth-associated phenotype.

Discussion

These studies provide insight into the roles that intra-tumor heterogeneity, transcriptional adaptation, and clonal evolution play as osteosarcoma cells colonize primary and metastatic tumor microenvironments. Using orthotopic cell line and PDX models of osteosarcoma, we show that tumor cells maintain transcriptional heterogeneity as they respond to changing microenvironment conditions while also plastically adapting their transcriptional profiles. We identified that primary and metastatic tumors demonstrate phenotypic heterogeneity where subsets of cells upregulate genes associated with distinct pathways, including glycolysis, hypoxia, EMT, and TNFα signaling via NFκB. We validated this functional heterogeneity for the identified pathways in publicly available patient primary tumor datasets. Furthermore, we validated our bioinformatics finding of metabolic heterogeneity using immunofluorescence staining and showed that heterogeneity in glycolysis activation is observed within individual metastatic lesions irrespective of lesion size and does not result from spatially isolated, metabolically distinct tumor regions. Finally, by combining lineage tracing and phenotype analysis, we identified that lung colonization enriches for specific clonal families that adopt a unique growth-associated phenotype. Put together, our studies suggest a tumor-intrinsic mechanism that allows for maintenance of phenotypic diversity, despite clonal selection, while undergoing adaptive transcriptional changes during lung colonization (***Figure 6***).

Developmental process in normal cells have been shown to maintain an overall degree of phenotypic heterogeneity(25,26). Congruently, osteoblast cells grown in cell culture demonstrated a baseline level of phenotypic heterogeneity. In contrast, our study identified that osteosarcoma cells, whether passaged in mice or cell culture, or exposed to selective pressures of tissue colonization, maintained a higher degree of phenotypic heterogeneity than normal osteoblast cells. Interestingly, the only sample that showed a decrease in phenotypic heterogeneity on lung colonization relative to the starting population was obtained from a patient with metastatic disease who received extensive chemotherapy, and hence was not representative

of cells that undergo early lung colonization. While more samples are needed to capture the true heterogeneity in osteosarcoma, one might speculate that normal developmental processes designed to maintain diverse phenotypes cooperate to support normal bone growth and that these cooperative mechanisms may provide a survival advantage in a transformed malignant state.

While pseudo-bulk analyses identified shared pathways associated with tibia and lung colonization across the models, single cell analysis identified that each tumor was composed of phenotypically distinct subsets associated with unique combinations of activated pathways. In this study, we validated our bioinformatics finding of heterogeneity in glycolytic activation by identifying correlated staining patterns for four distinct markers of glycolysis activation, namely GLUT1, HK2, CA9, MCT4(23), along with a known upstream regulator of GLUT1, MYC(24). We showed that this heterogeneity in glycolysis activation is intrinsic to individual metastatic lesions and not a result of spatially isolated metabolically distinct lesions. Strong correlation between stains for each of these five markers confirmed that the observed heterogeneity did not arise from stochastic gene expression changes. These findings also suggest that the Warburg effect is demonstrated by only certain subsets within a tumor. The Warburg effect is a well-known phenomenon in cancer cells(27,28), and our findings are in line with heterogeneous glycolysis activation reported in recent single cell sequencing studies in other cancers(29). Furthermore, we validated heterogeneous expression of genes associated with glycolysis and other pathways in publicly available single-cell RNA sequenced primary patient samples, confirming that our observations in immuno-deficient preclinical models of osteosarcoma holds true in patient samples. Overall, we validated our bioinformatics finding of heterogeneous activation of glycolysis in both primary and metastatic lesions and showed that tumor cells retain metabolic heterogeneity despite selective pressures during tissue colonization.

Combining the power of scRNA-seq with lineage tracing allowed us to make inferences about how clonal selection and transcriptional plasticity may contribute to the emergence of traits that

facilitate lung colonization. This approach allowed us to address previously unanswered questions regarding the relationship between clonality and phenotype. We showed that lung colonization enriches for multiple clonal families, wherein clonally related cells tend to have similar transcriptional profiles. In contrast, tumor cells retained clonal diversity on tibia colonization, suggesting that most cells that were injected intra-tibially survived and colonized the tibia. We acknowledge that the study design employed remains agnostic of the multi-step process required to effect metastasis in a patient. The design very simply asks whether the capacity to colonize these different tissues is contained within a few rare clones with a pre-existing phenotype or whether diverse groups of cells have the capacity to adapt to the stressors imposed by the tibia or lung environment. Our results suggest that both answers have some truth. The drastic shift in phenotype from cell culture or flank tumors to primary or metastatic tumors endorses the role of microenvironment cues in shaping tumor cell behavior. However, lung colonization enriched for specific clonal populations that all adopted a similar growth-associated phenotype. Genes differentially upregulated in the top ten enriched clonal families overlapped mostly with genes related to hypoxia and glycolysis. While hypoxia response is an important contributor to the Warburg effect(30,31), these observations show that this growth-associated phenotype is not adopted by the bulk of the metastatic tumor, but rather limited to clonal populations of cells that are enriched for during lung colonization. These findings corroborate recent efforts with single cell profiling of other cancers identifying metabolic heterogeneity(29). We recognize that our approach does not determine whether the enriched clones composed individual metastatic lesions, or whether different clones colonized individual lesions cooperatively, however, immunofluorescence staining for glycolysis markers suggested that this metabolic heterogeneity is likely inherent to individual lesions. While pseudo-bulk analyses identified genes associated with TNFα signaling via NFκB and EMT to be most significantly upregulated upon lung colonization (***Figure 2***C), differential gene expression analyses between the most enriched clones and remaining metastatic cells identified a distinct transcriptional program associated with

activation of glycolysis and hypoxia related genes. These data put together suggest that lung colonization is likely a two-step process - initial survival followed by expansion in a subset of cells that adopt a growth-associated phenotype distinct from the remaining bulk of the metastatic tumor cells.

Conclusions

Overall, we show that osteosarcoma cells maintained intra-tumor phenotypic heterogeneity despite plastic adaptions during tibia and lung colonization, and the process of lung colonization enriched for distinct clonal populations. Interestingly, phenotype within enriched clonal families were retained across multiple cell divisions. Whether this conservation of phenotype in cells that originated from a common ancestor has an underlying genetic or epigenetic basis remains a point of active study. Additionally, maintenance of range/degree of intra-tumor heterogeneity endorses the role of cell-autonomous mechanisms in holding up a very basic evolutionary advantage associated with maintaining diverse phenotypic states(32). How this transcriptional heterogeneity is regulated in osteosarcoma cells and if underlying genomic heterogeneity engenders transcriptional heterogeneity remain to be seen.

Methods

Experimental model - PDXs, Cell lines and murine studies.

Patient derived xenografts (PDXs). OS-17 PDX tissue was obtained from a primary femur biopsy performed at St. Jude's Children's Research Hospital in Memphis and was a gift from Peter Houghton(33). Patient-derived samples, NCH-OS-2 and NCH-OS-7 were obtained from patients consented under an Institutional Review Board (IRB)-approved protocol IRB11-00478 at Nationwide Children's Hospital (Human Subject Assurance Number 00002860).

Cell lines. OS-17 cells were derived from an early passage of the OS-17 PDX (see above). These cells were grown in RPMI (Corning, 10-040-CV) supplemented with 10% fetal bovine serum

(FBS). 143B cells were obtained from the American Type Culture Collection (ATCC, CRL-8303) and grown in DMEM (Corning, 10-013-CV) supplemented with 10% FBS. Human osteoblast cells (hFOB 1.19) were obtained from the American Type Culture Collection (ATCC, CRL-11372) and grown in DMEM (Corning, 10-013-CV) supplemented with 0.3 mg/ml G418 and 10% FBS. All cell lines were tested annually for both STR genotyping and mycoplasma contamination using testing services provided by Genetica.

Murine Studies. All animal studies were approved by Nationwide Children's Hospital Institutional Animal Care and Use Committee (IACUC protocol AR12-00074). *A. Flank.* Cryopreserved viable tissue pieces from OS-17, 143B, NCH-OS-2 and NCH-OS-7 PDX tumors were placed in the right flank of recipient C.B-17/IcrHsd-Prkdc^{scid} mice (Envigo, Frederick, MD). These subcutaneous tumors were allowed to grow to 300 mm3 before excision. These were then prepped for single-cell RNA-seq. *B. Orthotopic primary tumors.* Single cell suspensions of OS-17, 143B, NCH-OS-2 and NCH-OS-7 were injected intra-tibially in C.B-17/IcrHsd-Prkdc^{scid} mice as per IACUC guidelines. Primary tumors were excised once they grew to 800 mm3, and prepped for single-cell RNA-seq. *C. Experimental metastasis.* Single cell suspensions of OS-17, 143B, NCH-OS-2 and NCH-OS-7 were injected intra-venously in C.B-17/IcrHsd-Prkdc^{scid} mice. Lungs were harvested once these mice reached endpoint. Endpoint criteria for euthanasia was defined as weight loss of >10% or a body condition score (BCS) of <10. For fluorescence immunohistochemistry studies, tumors were placed in 10% formalin for 24 hours at 4°C, then moved to (phosphate-buffered saline) PBS for at least one hour at 4°C. Tissues were then placed in tissue cassettes and placed in fresh PBS. Tissues were embedded in paraffin.

Fluorescent immunohistochemistry

Antibodies against glucose transporter 1, hexokinase 2, and carbonic anhydrase 9 were purchased from Abcam (Cambridge, UK). An antibody against c-myc was purchased from Invitrogen (Carlsbad, CA, USA). An antibody against monocarboxylate transporter 4 was

purchased from Santa Cruz Biotechnology (Dallas, TX, USA). Antibodies against vimentin were purchased from Cell Signaling Technology (Danvers, MA, USA) and Abnova (Taipei, Taiwan). Anti-rabbit and mouse Alexa Fluor 488 antibodies, anti-rabbit and -mouse Alexa Fluor 568 antibodies, and DAPI (4, 6-diamidino-2-phenylindole dihydrochloride) were purchased from Invitrogen (Carlsbad, CA, USA).

Paraffin embedded tissues were cut into 4uM sections and placed on glass slides. The sections were deparaffinized with xylene and rehydrated. Sections were submerged into a Tris-EDTA solution (pH 9.0) or a citrate solution (pH 6.0) and heated for antigen retrieval. Sections were blocked and permeabilized with a solution of PBS + 0.2% triton + 2% bovine serum albumin for one hour at room temperature. Primary antibodies against glucose transporter 1 (Abcam, 1:200 dilutions), hexokinase 2 (3D3, Abcam, 1:10 dilutions), carbonic anhydrase 9 (2D3, Abcam, 1:100 dilutions), c-myc (9E10, Invitrogen, 1:100 dilutions), monocarboxylate transporter 4 (D-1, Santa Cruz Biotechnology, 1:50 dilutions), rabbit anti-human vimentin (D21H3 Cell Signaling Technology, 1:100 dilutions) and mouse anti-human vimentin (SRL33 Abnova, 1:200 dilutions) were diluted in PBS + 0.2% triton + 2% bovine serum albumin. The blocking solution was removed from slides and primary antibodies were applied to the sections overnight at 4°C. Sections were washed three times with PBS + 0.2% triton. All secondary antibodies and DAPI (Invitrogen) were diluted 1:500 in PBS + 0.2% triton + 2% bovine serum albumin and added to the samples for 1 hour at room temperature. Sections were washed three times with PBS + 0.2% triton, and once a final time with reverse osmosis water. Samples were mounted in an aqueous mountant (Invitrogen, Carlsbad, CA, USA). Each tissue section was co-stained for vimentin and one of the other markers of interest.

Whole-section multichannel images were captured using a Nikon Ti2-E motorized microscope with a Lumencor SOLA LED light engine (at 50% power), a Hamamatsu ORCA Fusion camera, and Nikon Plan Apochromat Lambda objectives using Nikon NIS-Elements AR version 5.30

software. Each sample was imaged at 10x magnification with a final 16-bit image resolution of 0.64 µm/pixel. Identical imaging settings were used for all samples within the same staining and imaging set.

Images were analyzed using Nikon NIS-Elements AR software version 5.30 with the General Analysis 3 module. Semi-automated tumor segmentation was performed based on vimentin staining, and the segmented regions were manually modified by an unbiased operator as needed to ensure specific and complete tumor selection. Images were then rescaled to 1.28 µm/pixel and the intensities of all pixels representing tumor tissue were recorded in a frequency table for each sample. For assessing correlation between non-vimentin markers, image channels representing each marker of interest from different tissue sections were aligned using the multimodal image registration tool. Following alignment, an intensity profile line of 2-3 mm in length was plotted through tumor regions showing diverse signal landscapes, and the intensities of pixels along the profile line were recorded for each marker. All marker intensities were plotted by distance along the profile line in GraphPad Prism software version 9.0.0, and the curves were smoothed using a 2nd order polynomial based on 50 neighboring points (25 on each side) to account for minor mismatches in image channels from different tissue sections. The Pearson correlation of each pair of markers was then calculated from the smoothed XY curves.

Single-cell RNA-Seq

Tumors harvested from mice were processed using the human tumor dissociation kit (Miltenyi Biotec, 130-095-929) with a GentleMacs Octo Dissociator with Heaters (Miltenyi Biotec, 130-096-427). Single cell suspensions in 0.04% BSA-PBS of cell lines, and dissociated tumor tissues were generated and run on Chromium Single Cell 3′RNA-sequencing system (10x Genomics) with the Reagent Kit v3 according to the manufacturer's instructions. Briefly, cells were loaded into Chromium Single Cell Chip v3 (10x Genomics) with a targeted cell recovery of 5,000 cells per sample. After performing cDNA purification, amplification, and library construction (sample index

PCR 14 cycles) as instructed, we sequenced sample libraries on a half lane of HS4000 (Illumina) to yield (after quality control) about 65,000 paired-end reads per cell.

Cellular Barcoding

We synthesized barcoded lentivirus library using CloneTracker XP™ 10M Barcode-3' Library with Venus-Puro (plasmid) (Cellecta, BCXP10M3VP-P) as described in Wang and McManus 2009 (34) with PEI as the transfection reagent. We infected OS-17 cells with in-house prepared virus library in the presence of Polybrene (8 µg/ml). The barcoded plasmids contain ~10M 38-bp semi-random oligonucleotide sequence that is captured on the Chromium Single Cell 3′RNA-sequencing system. 48 h post-infection, OS-17 cells were used to generate orthotopic primary and metastatic tumor models as described above.

Cellular Barcoding Computational Analysis

Raw sequencing data was pre-processed to extract the lineage tag (LT) using known flanking sequences, and the matching cell ID (CID). Lines without high-confidence cell ID assignment were removed and redundant reads were removed. The extracted LT barcode reads were matched against the know Cellecta barcode library. Reads with barcodes that didn't match the Cellecta library were eliminated. The LT barcode for each matching CID was integrated into the SEURAT object metadata to allow for further analysis (see below).

Single-cell RNA-Seq analysis

Cell Ranger version 3.0.2 (10x Genomics) was used to convert Illumina BCL files to FASTQ files. These FASTQ files were then de-multiplexed and aligned to the hg19 human reference genome provided by 10X Genomics, to generate gene-cell matrices. We used the SEURAT R package(35–37) for quality control, filtering, and analysis of the data. Cells were filtered to remove doublets (outliers with high count and high genes per cell), low quality cells (outliers with low count and low genes per cell), and cells with high mitochondrial genes (indicative of cells with broken

membrane). Cells with fewer than 800 expressed genes and genes expressed in fewer than 5 cells were filtered out. The total numbers of cells in each model after filtering were as follows: Osteoblasts (cell culture): 5735; OS-17 (cell culture): 3,178; OS-17 (tibia): 4,574; OS-17(lung): 2,849; 143B (cell culture): 3,354; 143B (tibia): 6,187; 143B (lung): 5,134; NCH-OS-2 (flank): 6,749; NCH-OS-2 (tibia): 4,285; NCH-OS-2 (lung): 1,645; NCH-OS-7 (flank): 1,998; NCH-OS-7 (tibia): 2,891; NCH-OS-7 (lung): 5,133. In analyses that required comparison across conditions or models, samples were subset to contain equal numbers of cells and this number is specified in the figure legends. We transformed and normalized unique molecular identifier (UMI) counts using the 'NormalizeData' function in SEURAT package version 4.0.2(38) with default parameters. We mitigated the effects of cell cycle heterogeneity by regressing out canonical G2/M- and S-Phase genes using the 'ScaleData' function in SEURAT. Principle component analysis (PCA) was performed using the top 2,000 highly variable genes identified by the SEURAT function 'FindVariableFeatures' with default parameters. For each dataset, the first twenty principal components were selected based on the elbow plot for percentage explained variances, representing ~55.5–60.3% of total variances. The UMAP transformation(39) was performed on selected principal components using the 'RunUMAP' function. We applied shared nearest neighbor (SNN) modularity optimization(40) for clustering. We calculated silhouette scores for different number of clusters (from two clusters to ten clusters) to measure how similar one cell was to other cells in its own cluster compared with other clusters using the silhouette function in the R package cluster. We determined the optimum number of clusters for each sample by maximizing the Silhouette score. Datasets were integrated using four different approaches (FastMNN(41), SCTransform(42), Harmony(43), merge Seurat objects(44)) to determine the optimal method. PCA using the expression of cell cycle genes identified that integrating datasets with 'merge' function in SEUART or application of Harmony gave consistent results where cells did not cluster by cell cycle.

Marker genes were identified for each cluster relative to other clusters using the 'FindMarkers' function, returning only positive markers, with 'test.use' set to DESeq2(45) which uses a negative binomial distribution. Pathway enrichment analysis was performed on these markers genes using the enricher function in the R package clusterProfiler(46) with default parameters with msigdb Hallmark gene sets(47). Pseudo-bulk analysis was performed by setting identities of each cell to the sample. We identified gene differentially regulated using the 'FindMarkers' function for both positive and negative markers upon tibia or lung colonization. Pathway enrichment analysis was performed on these markers as described above. The ITH score was calculated as described in Stewart et al.(18) Briefly, it was defined as the average Euclidean distance between each cell to every other cell in each sample, in terms of the selected principal components.

We downloaded validation datasets from Gene Expression Omnibus (GEO) for seven patient primary tumor tissues published in a recent study (GEO accession number-GSE152048)(16). We used the Seurat R package(35–37) for quality control, filtering, and analysis of these gene expression matrices. Cells were filtered to remove doublets, low quality cells, and cells with high mitochondrial genes as described above. Cells with fewer than 800 expressed genes and genes expressed in fewer than 5 cells were filtered out. We transformed and normalized UMI counts using the 'NormalizeData' function in SEURAT package version 4.0.2(38) with default parameters. Principle component analysis (PCA) was performed using the top 2,000 highly variable genes identified by the SEURAT function 'FindVariableFeatures' with default parameters. Using the marker gene sets used in the paper(16), we separated tumor cells from patient host cells. For each sample, the first twenty principal components were selected based on the elbow plot for percentage explained variances, representing ~51.8–61.5% of total variances. The UMAP transformation(39) was performed on selected principal components using the 'RunUMAP' function. Module scores for Glycolysis, Hypoxia, EMT, TNFα signaling via NFκB were calculated

using the ‘AddModuleScore’ function in SEURAT with corresponding Hallmark msigdb gene sets as input features for the expression program.

Statistical analysis

Statistical analyses were performed using R software environment for statistical computing(48) and Prism 9 (GraphPad Software, Inc.). The packages used in R software are mentioned through the text in the methods section. For differential gene expression analysis, a negative binomial model (DESeq2)(45) was used. For multiple testing, p values were adjusted using Benjamini Hochberg (BH) correction. For ITH score comparisons, data were subjected to one-way analysis of variance (ANOVA) followed by Šidák multiple comparisons test.

Abbreviations

PDX: patient-derived xenograft

ITH: intra-tumor heterogeneity

EMT: epithelial to mesenchymal transition

MTORC1: mechanistic target of rapamycin (mTOR) complex 1.

PI3K: Phosphoinositide 3-kinase

AKT: Protein kinase B

TGF: Transforming growth-factor

TNFα: tumor necrosis factor α

NFKB: Nuclear Factor kappa-light-chain-enhancer of activated B cells

Declarations

Ethics approval and consent to participate

Patient-derived samples were obtained from patients consented under an Institutional Review Board (IRB)-approved protocol IRB11-00478 at Nationwide Children's Hospital (Human Subject Assurance Number 00002860).

All animal studies were approved by Nationwide Children's Hospital Institutional Animal Care and Use Committee (IACUC protocol AR12-00074).

Consent for publication

Not applicable

Availability of data and materials

The datasets supporting the conclusions of this article are available in the NCBI's Gene Expression Omnibus (GEO) repository, [https://www.ncbi.nlm.nih.gov/geo/query/acc.cgi?acc=GSE179681].

Code availability

The bioinformatics analyses were performed using open-source software, including SEURAT version 4.0.2(38), clusterProfiler version 3.14.3(46), and Cell Ranger version 3.0.2. All code is deposited in https://github.com/kidcancerlab/OSHetero2021.

Competing interests

The authors declare that they have no competing interests

Acknowledgements

We would like to thank our funding sources. This work was generously supported by funding provided by NIH/NCI (K08CA201638, RDR), St Baldrick's Foundation Scholar Award (RDR), Hyundai Hope on Wheels Young Investigator Award (RDR), CancerFree KIDS Foundation (RDR), Steps for Sarcoma Foundation (RDR), Sarcoma Foundation of America (RDR), a Pelotonia

Fellowship (SR), a Nationwide Children's Director's Strategic Development Fund, and an NIH CTSA Grant UL1TR002733.

Authors' contributions

SR and RDR conceived and designed the study. SR and RDR developed the methodology. MC and ACG prepared libraries for next-generation sequencing. SR, CT, MW, MVC, AO and EF performed computation analysis. CAM performed Immuno-fluorescence staining. TAV and KMF supported image acquisition and analysis of immunofluorescence experiments. SR and RDR interpreted all the consolidated data and wrote the manuscript. SR, CAM and RDR edited the manuscript. All authors read and approved the final manuscript.

References

1. Casali PG, Bielack S, Abecassis N, Aro HT, Bauer S, Biagini R, et al. Bone sarcomas: ESMO-PaedCan-EURACAN Clinical Practice Guidelines for diagnosis, treatment and follow-up. Ann Oncol. 2018;29(August):iv79–95.

2. Savage SA, Mirabello L. Using epidemiology and genomics to understand osteosarcoma etiology. Sarcoma. 2011;2011:14–6.

3. Lindsey BA, Markel JE, Kleinerman ES. Osteosarcoma Overview. Rheumatol Ther. 2017 Jun;4(1):25–43.

4. Geller DS, Gorlick R. Osteosarcoma: a review of diagnosis, management, and treatment strategies. Clin Adv Hematol Oncol. 2010 Oct;8(10):705–18.

5. Link MP, Goorin AM, Miser AW, Green AA, Pratt CB, Belasco JB, et al. The Effect of Adjuvant Chemotherapy on Relapse-Free Survival in Patients with Osteosarcoma of the Extremity. N Engl J Med [Internet]. 1986 Jun 19 [cited 2021 Jun 7];314(25):1600–6. Available from: https://pubmed.ncbi.nlm.nih.gov/3520317/

6. Fan TM, Roberts RD, Lizardo MM. Understanding and Modeling Metastasis Biology to Improve Therapeutic Strategies for Combating Osteosarcoma Progression. Vol. 10, Frontiers in Oncology. Frontiers Media S.A.; 2020.

7. Aljubran AH, Griffin A, Pintilie M, Blackstein M. Osteosarcoma in adolescents and adults: Survival analysis with and without lung metastases. Ann Oncol. 2009 Jun 1;20(6):1136–41.

8. Khanna C, Fan TM, Gorlick R, Helman LJ, Kleinerman ES, Adamson PC, et al. Toward a drug development path that targets metastatic progression in osteosarcoma. Clin cancer Res an Off J Am Assoc Cancer Res. 2014 Aug;20(16):4200–9.

9. Gambera S, Abarrategi A, González-Camacho F, Morales-Molina Á, Roma J, Alfranca A, et al. Clonal dynamics in osteosarcoma defined by RGB marking. Nat Commun. 2018;9(1).

10. OS B, H H, G S, S S, O F. Hematogenous micrometastases in osteosarcoma patients. Clin Cancer Res [Internet]. 2005 Jul 1 [cited 2021 Sep 3];11(13):4666–73. Available from: https://pubmed.ncbi.nlm.nih.gov/16000559/

11. S V, RA W. Tumor metastasis: molecular insights and evolving paradigms. Cell [Internet]. 2011 Oct 14 [cited 2021 Sep 3];147(2):275–92. Available from: https://pubmed.ncbi.nlm.nih.gov/22000009/

12. S T, C S. Metastasis as an evolutionary process. Science [Internet]. 2016 Apr 8 [cited 2021 Sep 3];352(6282):169–75. Available from: https://pubmed.ncbi.nlm.nih.gov/27124450/

13. Sethi N, Kang Y. Unravelling the complexity of metastasis — molecular understanding and targeted therapies. Nat Rev Cancer 2011 1110 [Internet]. 2011 Sep 23 [cited 2021

Sep 3];11(10):735–48. Available from: https://www.nature.com/articles/nrc3125

14. S V, J M. Origins of metastatic traits. Cancer Cell [Internet]. 2013 Oct 14 [cited 2021 Sep 3];24(4):410–21. Available from: https://pubmed.ncbi.nlm.nih.gov/24135279/

15. M C, GT B, MJ E, A S, J M, MC M, et al. Circulating tumor cells, disease progression, and survival in metastatic breast cancer. N Engl J Med [Internet]. 2004 Aug 19 [cited 2021 Sep 3];351(8):781–91. Available from: https://pubmed.ncbi.nlm.nih.gov/15317891/

16. Zhou Y, Yang D, Yang Q, Lv X, Huang W, Zhou Z, et al. Single-cell RNA landscape of intratumoral heterogeneity and immunosuppressive microenvironment in advanced osteosarcoma. Nat Commun [Internet]. 2020 Dec 1 [cited 2021 Mar 2];11(1):1–17. Available from: https://doi.org/10.1038/s41467-020-20059-6

17. Liu Y, Feng W, Dai Y, Bao M, Yuan Z, He M, et al. Single-Cell Transcriptomics Reveals the Complexity of the Tumor Microenvironment of Treatment-Naive Osteosarcoma. Front Oncol. 2021 Jul 21;0:2818.

18. Chalishazar MD, Moran C, Kalhor N, Stewart J, Tran H, Swisher SG, et al. Single-cell analyses reveal increased intratumoral heterogeneity after the onset of therapy resistance in small-cell lung cancer. Nat cancer. 2020;(614).

19. Yu X, Yustein JT, Xu J. Research models and mesenchymal/epithelial plasticity of osteosarcoma. Cell Biosci 2021 111 [Internet]. 2021 May 22 [cited 2021 Sep 5];11(1):1–12. Available from: https://cellandbioscience.biomedcentral.com/articles/10.1186/s13578-021-00600-w

20. Sun X, Yu Q. Intra-tumor heterogeneity of cancer cells and its implications for cancer treatment. Acta Pharmacol Sin 2015 3610 [Internet]. 2015 Sep 21 [cited 2021 Aug 31];36(10):1219–27. Available from: https://www.nature.com/articles/aps201592

21. Yoshioka H, Okita S, Nakano M, Minamizaki T, Nubukiyo A, Sotomaru Y, et al. Single-Cell RNA-Sequencing Reveals the Breadth of Osteoblast Heterogeneity. JBMR Plus [Internet]. 2021 Jun 1 [cited 2021 Aug 31];5(6). Available from: /pmc/articles/PMC8216137/

22. Sayles LC, Breese MR, Koehne AL, Leung SG, Lee AG, Liu HY, et al. Genome-informed targeted therapy for osteosarcoma. Cancer Discov [Internet]. 2019 Jan 1 [cited 2020 Nov 17];9(1):46–63. Available from: www.aacrjournals.org

23. Kim M-J, Kim D-H, Jung W-H, Koo J-S. Expression of metabolism-related proteins in triple-negative breast cancer. Int J Clin Exp Pathol. 2014;7(1):301–12.

24. CV D, A L, P G. MYC-induced cancer cell energy metabolism and therapeutic opportunities. Clin Cancer Res [Internet]. 2009 Nov 1 [cited 2021 Aug 31];15(21):6479–83. Available from: https://pubmed.ncbi.nlm.nih.gov/19861459/

25. Altschuler SJ, Wu LF. Cellular Heterogeneity: Do Differences Make a Difference? [Internet]. Vol. 141, Cell. Elsevier; 2010 [cited 2020 Jul 30]. p. 559–63. Available from: http://www.cell.com/article/S0092867410004873/fulltext

26. Chang HH, Hemberg M, Barahona M, Ingber DE, Huang S. Transcriptome-wide noise controls lineage choice in mammalian progenitor cells. Nature [Internet]. 2008 May 22 [cited 2020 Sep 6];453(7194):544–7. Available from: https://www.nature.com/articles/nature06965

27. RJ D, JJ L, G H, CB T. The biology of cancer: metabolic reprogramming fuels cell growth and proliferation. Cell Metab [Internet]. 2008 Jan 9 [cited 2021 Aug 31];7(1):11–20. Available from: https://pubmed.ncbi.nlm.nih.gov/18177721/

28. PP H, DM S. Cancer cell metabolism: Warburg and beyond. Cell [Internet]. 2008 Sep 5

[cited 2021 Aug 31];134(5):703–7. Available from: https://pubmed.ncbi.nlm.nih.gov/18775299/

29. Xiao Z, Dai Z, Locasale JW. Metabolic landscape of the tumor microenvironment at single cell resolution. Nat Commun 2019 101 [Internet]. 2019 Aug 21 [cited 2021 Aug 31];10(1):1–12. Available from: https://www.nature.com/articles/s41467-019-11738-0

30. Nakazawa MS, Keith B, Simon MC. Oxygen availability and metabolic adaptations. Nat Rev Cancer 2016 1610 [Internet]. 2016 Sep 23 [cited 2021 Sep 5];16(10):663–73. Available from: https://www.nature.com/articles/nrc.2016.84

31. Gatenby RA, Gillies RJ. Why do cancers have high aerobic glycolysis? Nat Rev Cancer 2004 411 [Internet]. 2004 Nov [cited 2021 Sep 5];4(11):891–9. Available from: https://www.nature.com/articles/nrc1478

32. Marusyk A, Polyak K. Tumor heterogeneity: causes and consequences. Biochim Biophys Acta [Internet]. 2010 Jan [cited 2020 Sep 6];1805(1):105–17. Available from: /pmc/articles/PMC2814927/?report=abstract

33. Houghton PJ, Morton CL, Tucker C, Payne D, Favours E, Cole C, et al. The pediatric preclinical testing program: Description of models and early testing results. Pediatr Blood Cancer. 2007;

34. Wang X, McManus M. Lentivirus production. J Vis Exp [Internet]. 2009 Oct 2 [cited 2019 Jul 21];(32). Available from: http://www.ncbi.nlm.nih.gov/pubmed/19801965

35. Satija R, Farrell JA, Gennert D, Schier AF, Regev A. Spatial reconstruction of single-cell gene expression data. Nat Biotechnol. 2015 May 12;33(5):495–502.

36. Haber AL, Biton M, Rogel N, Herbst RH, Shekhar K, Smillie C, et al. A single-cell survey of the small intestinal epithelium. Nature. 2017 Nov 16;551(7680):333–9.

37. Macosko EZ, Basu A, Satija R, Nemesh J, Shekhar K, Goldman M, et al. Highly parallel genome-wide expression profiling of individual cells using nanoliter droplets. Cell. 2015 May 30;161(5):1202–14.

38. Stuart T, Butler A, Hoffman P, Hafemeister C, Papalexi E, Mauck WM 3rd, et al. Comprehensive Integration of Single-Cell Data. Cell. 2019 Jun;177(7):1888-1902.e21.

39. McInnes L, Healy J, Melville J. UMAP: Uniform Manifold Approximation and Projection for Dimension Reduction. 2018 Feb 9 [cited 2021 Aug 31]; Available from: https://arxiv.org/abs/1802.03426v3

40. Waltman L, van Eck NJ. A smart local moving algorithm for large-scale modularity-based community detection. Eur Phys J B 2013 8611 [Internet]. 2013 Nov 13 [cited 2021 Aug 31];86(11):1–14. Available from: https://link.springer.com/article/10.1140/epjb/e2013-40829-0

41. Haghverdi L, Lun ATL, Morgan MD, Marioni JC. Batch effects in single-cell RNA-sequencing data are corrected by matching mutual nearest neighbors. Nat Biotechnol 2018 365 [Internet]. 2018 Apr 2 [cited 2021 Sep 6];36(5):421–7. Available from: https://www.nature.com/articles/nbt.4091

42. Hafemeister C, Satija R. Normalization and variance stabilization of single-cell RNA-seq data using regularized negative binomial regression. Genome Biol 2019 201 [Internet]. 2019 Dec 23 [cited 2021 Sep 6];20(1):1–15. Available from: https://genomebiology.biomedcentral.com/articles/10.1186/s13059-019-1874-1

43. Korsunsky I, Millard N, Fan J, Slowikowski K, Zhang F, Wei K, et al. Fast, sensitive and accurate integration of single-cell data with Harmony. Nat Methods 2019 1612 [Internet]. 2019 Nov 18 [cited 2021 Sep 6];16(12):1289–96. Available from: https://www.nature.com/articles/s41592-019-0619-0

44. merge: Merge Two Data Frames [Internet]. [cited 2021 Sep 6]. Available from: https://rdrr.io/r/base/merge.html

45. Love MI, Huber W, Anders S. Moderated estimation of fold change and dispersion for RNA-seq data with DESeq2. Genome Biol 2014 1512 [Internet]. 2014 Dec 5 [cited 2021 Aug 31];15(12):1–21. Available from: https://genomebiology.biomedcentral.com/articles/10.1186/s13059-014-0550-8

46. Yu G, Wang LG, Han Y, He QY. ClusterProfiler: An R package for comparing biological themes among gene clusters. Omi A J Integr Biol. 2012 May 1;16(5):284–7.

47. A L, A S, R P, H T, P T, JP M. Molecular signatures database (MSigDB) 3.0. Bioinformatics [Internet]. 2011 Jun [cited 2021 Aug 8];27(12):1739–40. Available from: https://pubmed.ncbi.nlm.nih.gov/21546393/

48. Foundation TR. The R Project for Statistical Computing [Internet]. [cited 2020 Jun 5]. Available from: https://www.r-project.org/

49. Tirosh I, Izar B, Prakadan SM, Wadsworth MH, Treacy D, Trombetta JJ, et al. Dissecting the multicellular ecosystem of metastatic melanoma by single-cell RNA-seq. Science (80-). 2016;352(6282):189–96.

Figures

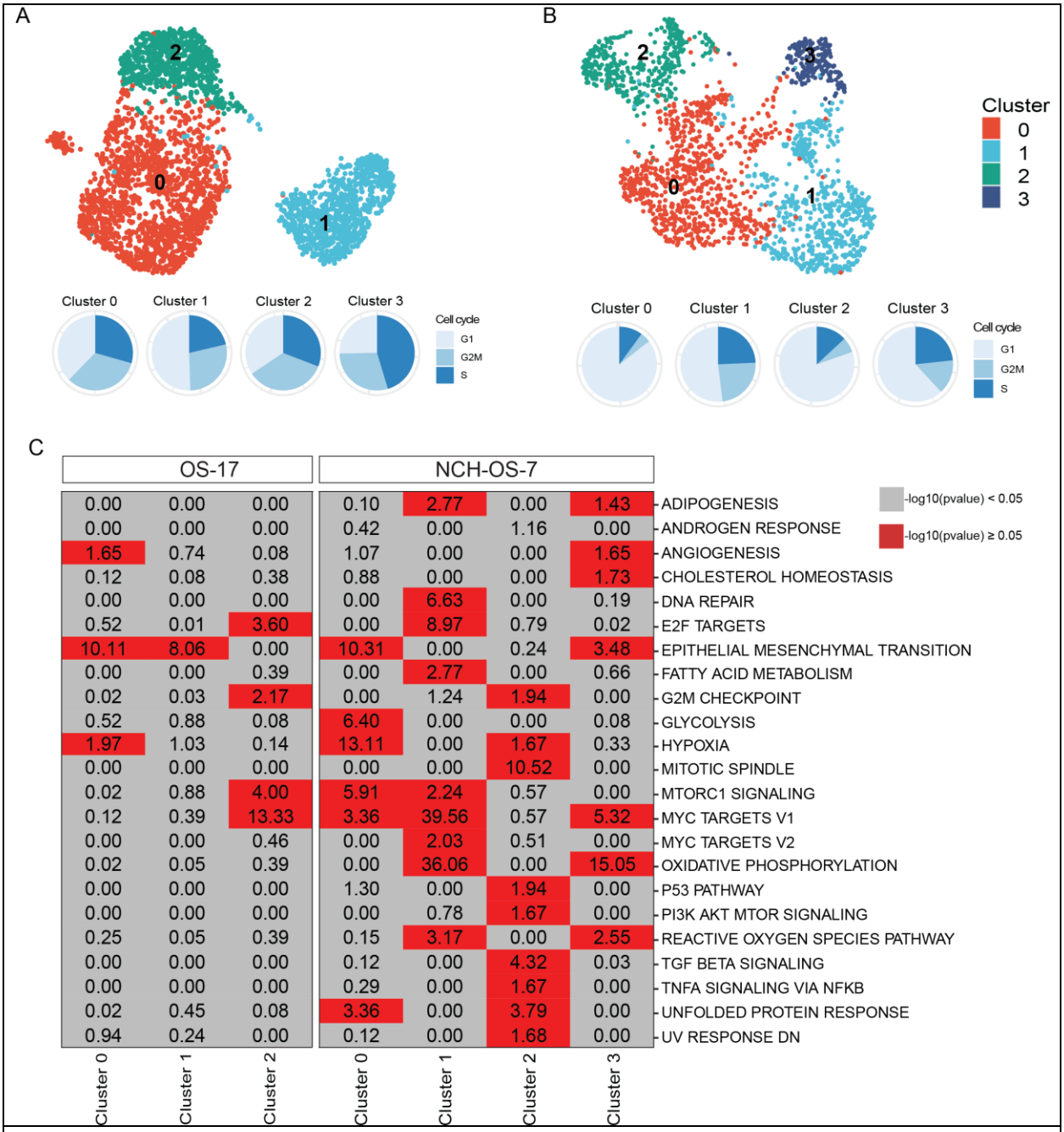

Figure 1. **Cell line and PDX models of osteosarcoma display transcriptional heterogeneity.** A) UMAP analysis of OS-17 cells (n = 3178) grown in cell culture. Cell cycle distribution of cells (n = 3178) is visualized as pie charts. B) UMAP analysis of NCH-OS-7 cells (n = 1998) grown as subcutaneous flank tumor. Cell cycle distribution of cells is visualized as pie charts. C) Pathway enrichment analysis for hallmark gene sets associated with genes upregulated in distinct clusters identified in the two osteosarcoma models. P values were adjusted for multiple comparisons. Boxes in grey identify non-significant enrichments, whereas boxes in red identify statistically significant enrichments. MTORC1: mechanistic target of rapamycin (mTOR) complex 1. PI3K: Phosphoinositide 3-kinase. AKT: Protein kinase B. TGF:

Transforming growth-factor. TNF: tumor necrosis factor. NFKB: Nuclear Factor kappa-light-chain-enhancer of activated B cells.

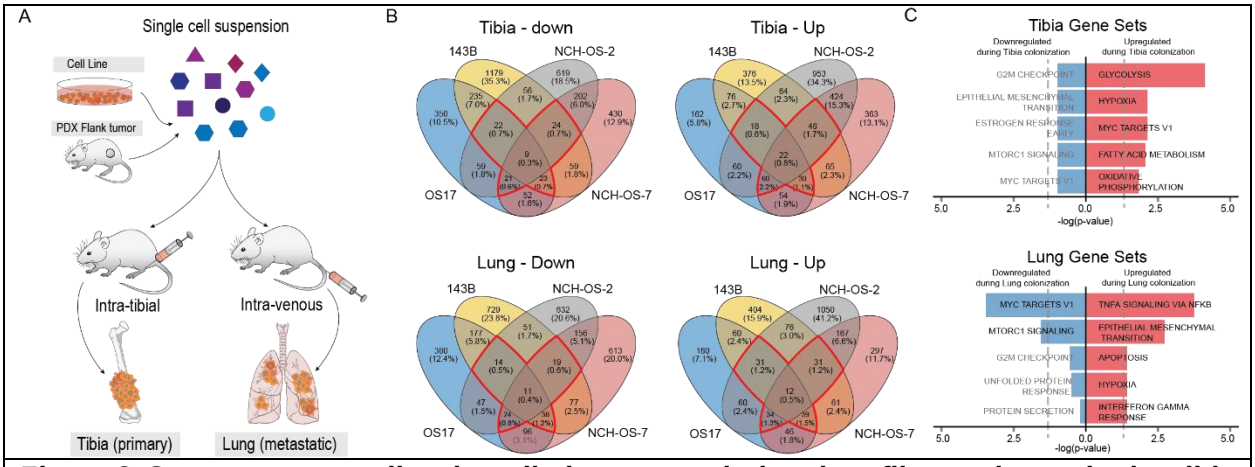

Figure 2. **Osteosarcoma cells adopt distinct transcriptional profiles as they colonize tibia and lung microenvironments.** A) Schematic of study design depicting generation of orthotopic primary and metastatic tumors. Tumors were harvested for scRNA-seq when mice reached endpoint. B) Venn diagrams showing overlap of differentially expressed genes that are up- or down- regulated in primary or metastatic tumors relative to corresponding starting population of cells (cell line or PDX flank tumors). Region outlined in red identifies differentially expressed genes shared across at least three models. C) Pathway enrichment analysis with adjusted p values for hallmark gene sets associated with these shared genes.

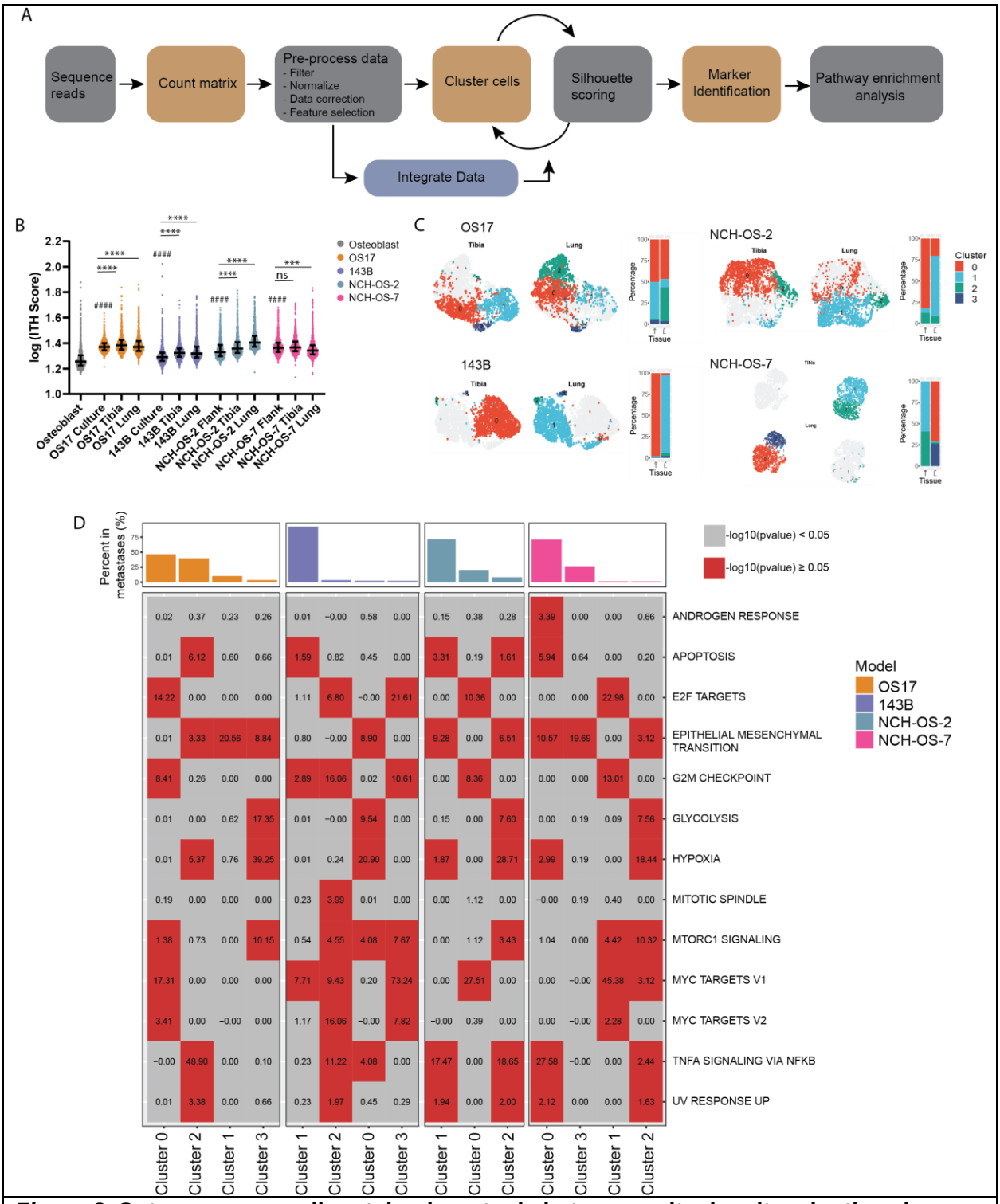

Figure 3. **Osteosarcoma cells retain phenotypic heterogeneity despite adaptive changes in response to changing microenvironments.** A) Schematic outlining scRNA-seq bioinformatics workflow. B) Osteosarcoma cells exhibited higher ITH scores than that of osteoblasts grown in cell culture (####p <0.001). Within model comparison, identified increase in ITH scores as cells colonize tibia and lung microenvironments, with the exception of NCH-OS-7 (****p <0.001). P values were adjusted using Šidák multiple comparisons test. C) UMAP

analysis for merged primary and metastatic samples in each of the four models. Cells in grey represent remaining cells in merged sample. Cluster enrichment analysis shows distribution of cells in each cluster in the two microenvironment conditions (tibia, lung). While some cells in the primary and metastatic lesions adopted shared phenotypes, others adopted distinct phenotypes. D) Metabolic heterogeneity in glycolysis activation. We used a pathway enrichment analysis for hallmark gene sets using genes differentially upregulated in each cluster relative to every other cluster within the same model. P values were adjusted for multiple comparisons. Boxes in grey identify non-significant pathway enrichments, whereas boxes in red identify statistically significant enrichments. Bar plot shows percentage of cells identified per cluster in lung metastases. In B-D, samples subset to equal number of cells to allow inter-model comparison (n=1500 per condition).

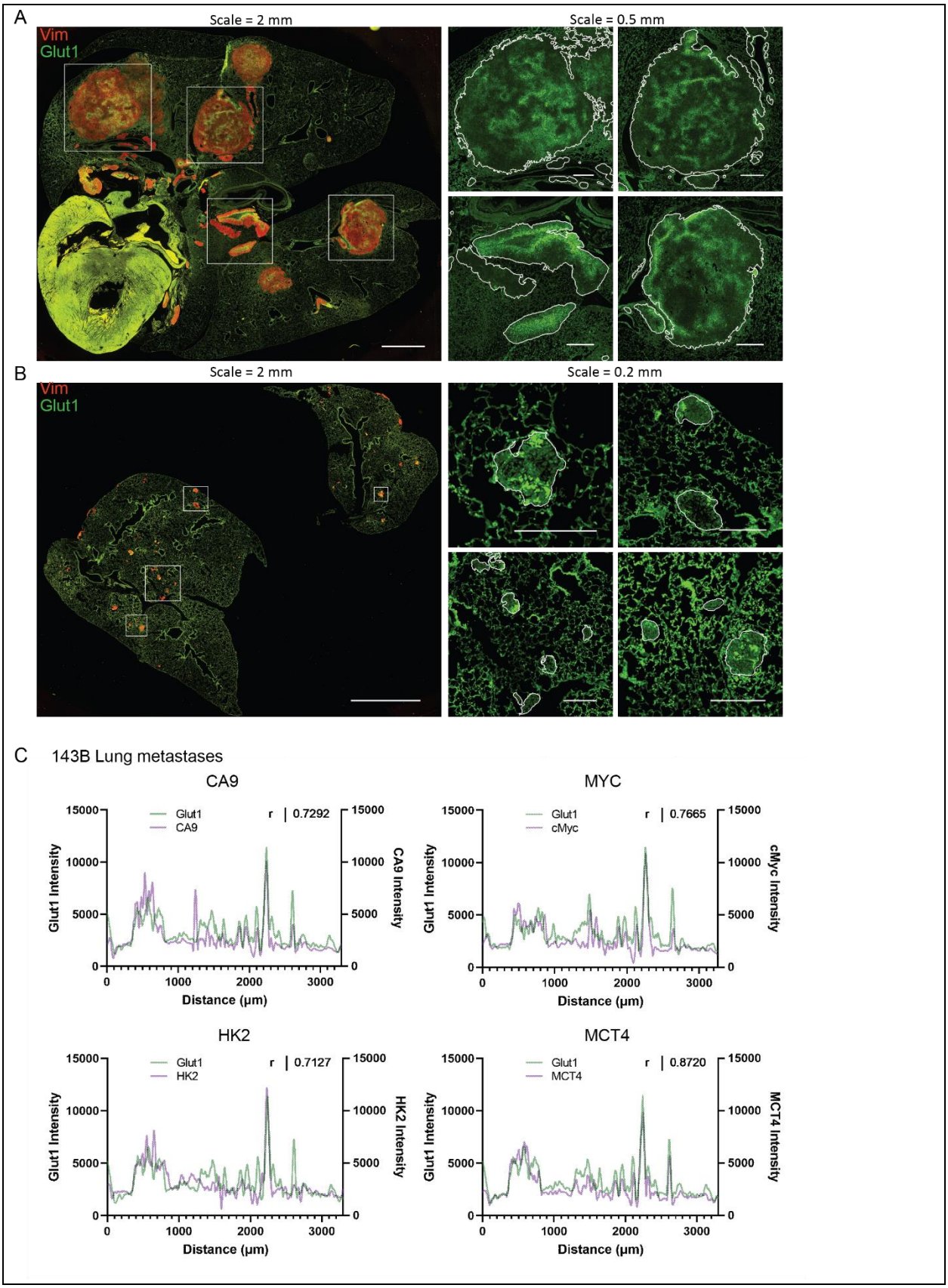
A
Scale = 2 mm
Vim
Glut1
Scale = 0.5 mm
B
Scale = 2 mm
Vim
Glut1
Scale = 0.2 mm
C
143B Lung metastases
CA9
Glut1
CA9
r | 0.7292
Glut1 Intensity
CA9 Intensity
Distance (µm)
MYC
Glut1
cMyc
r | 0.7665
Glut1 Intensity
cMyc Intensity
Distance (µm)
HK2
Glut1
HK2
r | 0.7127
Glut1 Intensity
HK2 Intensity
Distance (µm)
MCT4
Glut1
MCT4
r | 0.8720
Glut1 Intensity
MCT4 Intensity
Distance (µm)

Figure 4. **Heterogeneity in Glycolysis activation identified within metastatic osteosarcoma lesions.** A, B) Immunofluorescence staining of mouse lungs bearing OS-17 and 143B metastatic tumors, respectively, for GLUT1 (green; a marker of glycolysis) and vimentin (red; marker to identify osteosarcoma cells). Magnified GLUT1 staining is shown for the boxed regions on the whole-section images. Lesion edges are indicated by white outlines in the magnified regions. Tumors showed a high degree of intra-tumor variation in GLUT1 staining intensity. C) Correlation of fluorescence intensity of markers of glycolysis (CA9, HK2, MCT4) and an upstream regulator (MYC) with GLUT1 along a ~3mm profile line drawn through the lesions. The location and intensity of staining was highly correlated with GLUT1 for all markers. Representative of n=3 mice

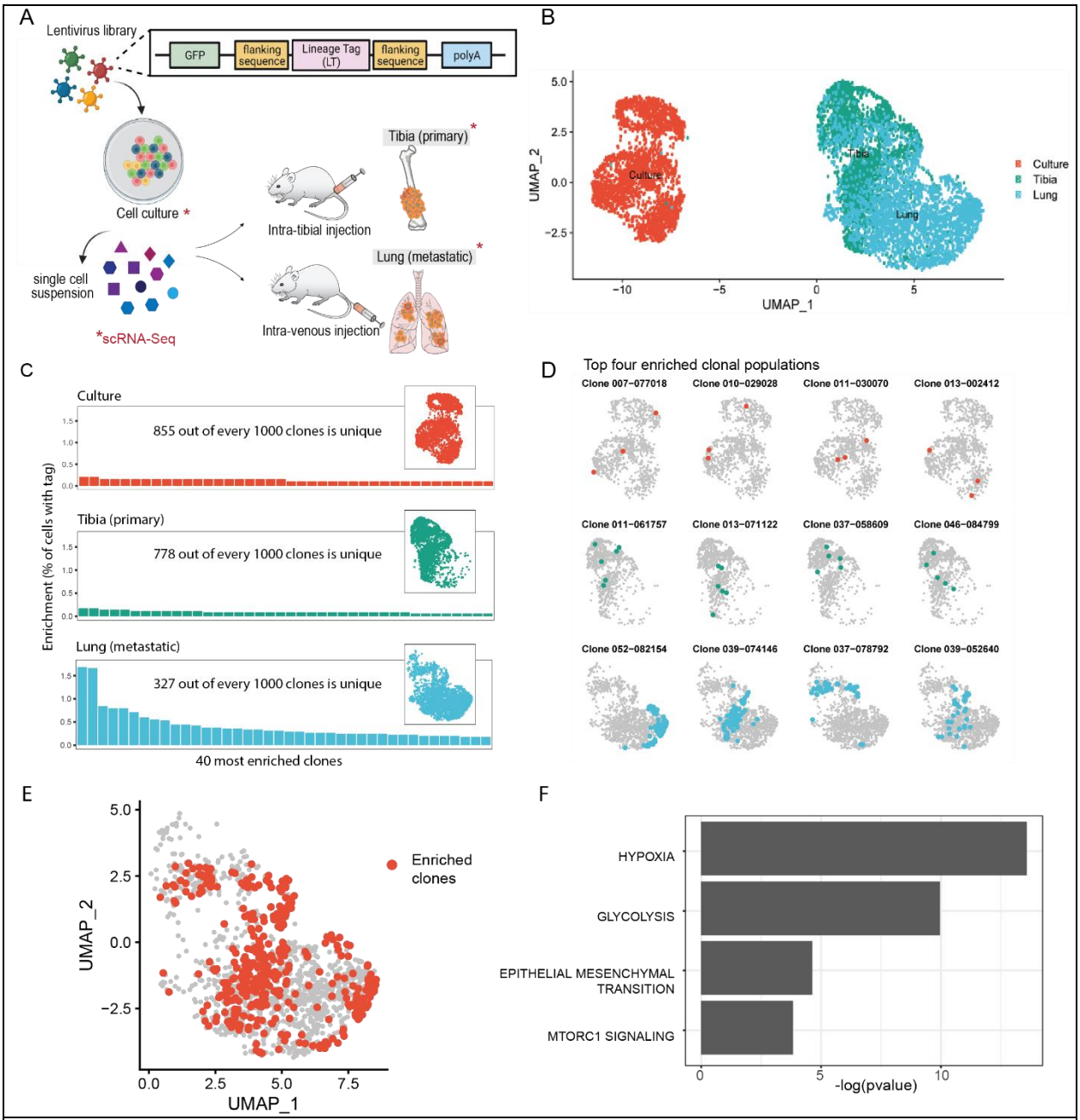

Figure 5. **Lung colonization bottleneck enriches for clonal populations with a common transcriptional phenotype.** A) Schematic of experimental set-up. B) UMAP analysis of lineage tagged OS-17 cells in culture, implanted into tibia, or inoculated to generate lung metastases. These lineage tags are heritable allowing us to track the transcriptional profiles of daughter cells originating from the same ancestor. Metastatic and orthotopic samples share many cells with similar phenotypes, though cultured cells are dramatically different (n = 2800 per condition) C) Frequency distribution of clones identified in each of the conditions. A high level of clonal diversity is maintained in the orthotopic tumors (78% unique clones in primary tumor compared to 86% unique clones in cell culture); though dominant clones emerge in the lung (only 33% unique clones). D) Overlay of cells sharing a common ancestor onto the dimensional reduction plots in the top four enriched clonal families. E) UMAP visualization of cells belonging to top ten enriched clonal families highlighted in red. F) Pathway enrichment analysis for hallmark gene

sets comparing enriched clones relative to the remaining metastatic tumor cells identifies Hypoxia, Glycolysis, EMT and MTORC1 signaling related genes to be significantly upregulated.

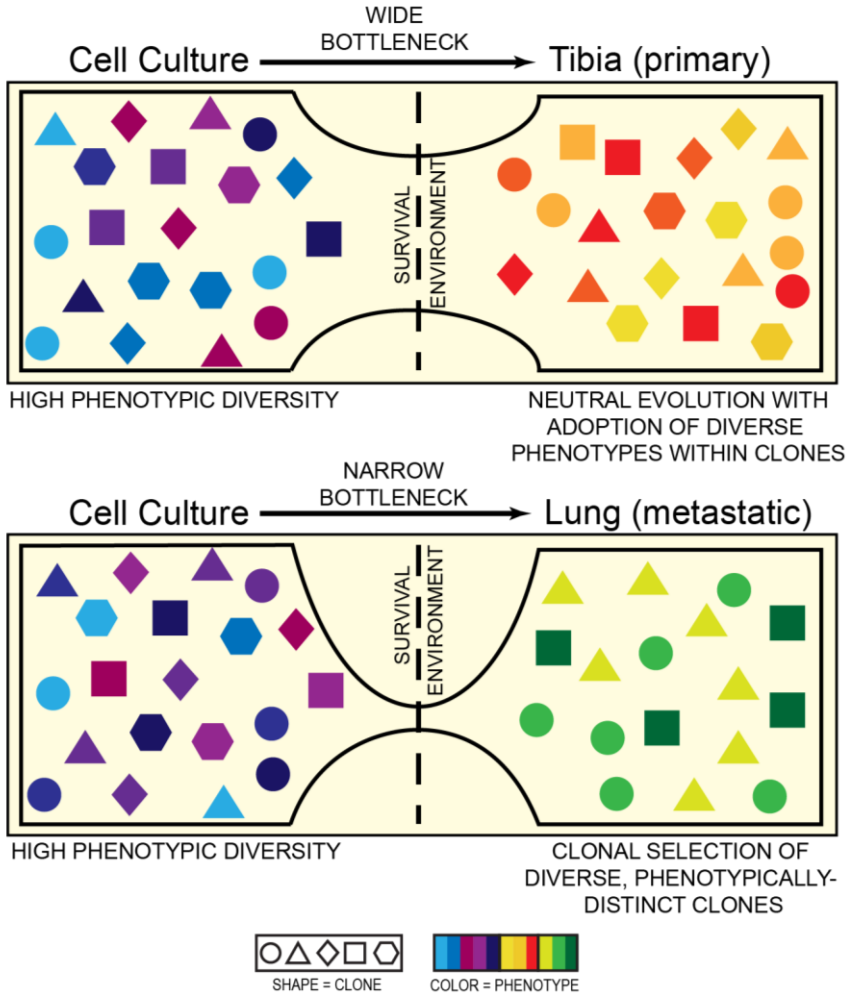

Figure 6. **Schematic of tumor cell adaptation to changing microenvironments.** Osteosarcoma cells demonstrate high transcriptional heterogeneity (colors) in cell culture, orthotopic tibia and lung microenvironments. Tumors that grow in the orthotopic primary lesions follow dynamics of neutral evolution where different cancer clones (shapes) co-exist and propagate simultaneously. The selective pressure of lung colonization results in enrichment of clonal families with different phenotypes (colors), where cells belonging to the same family (shape) tend to have similar phenotypes (color).

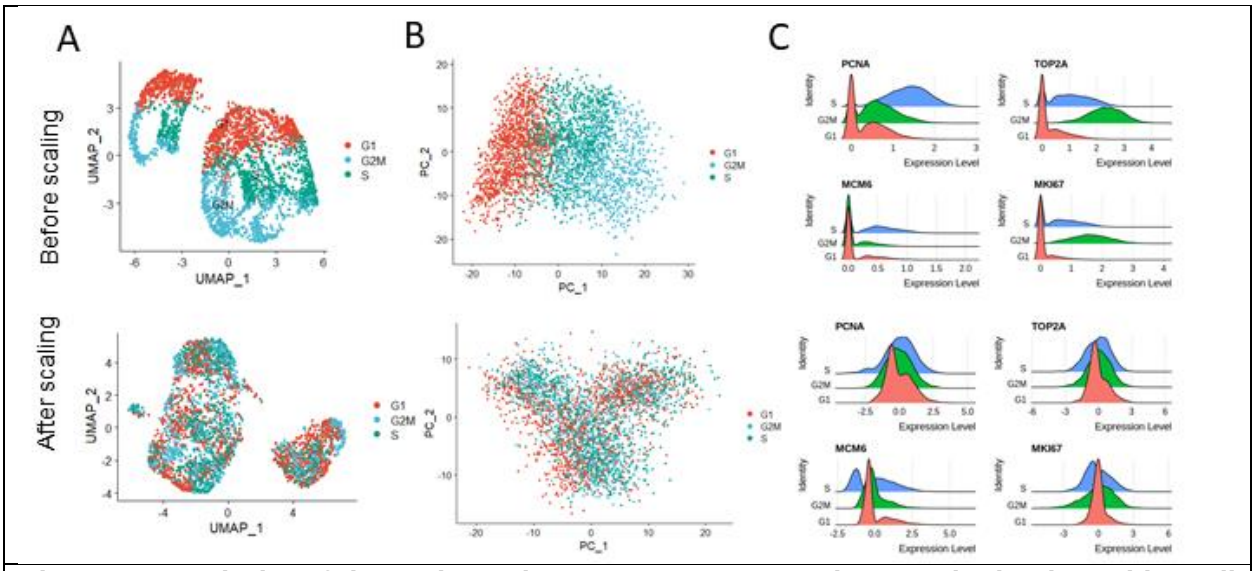

Figure S 1. **Majority of the variance in our osteosarcoma datasets is dominated by cell cycle associated genes.** OS-17 cells were scored based on expression of G2/M and S phase markers, described in Tirosh et al. 2016(49). A) UMAP analysis and B) PCA on cell cycle genes before cell cycle regression reveals that cells separate entirely by phase, confirmed using B) Ridge plots visualizing the distribution of cell cycle markers. After regressing out cell cycle scores, UMAP analysis and PCA on cell cycle genes show that cells no longer separate by phase. This is confirmed using Ridge plots of cell cycle markers. These plots are representative of all datasets.

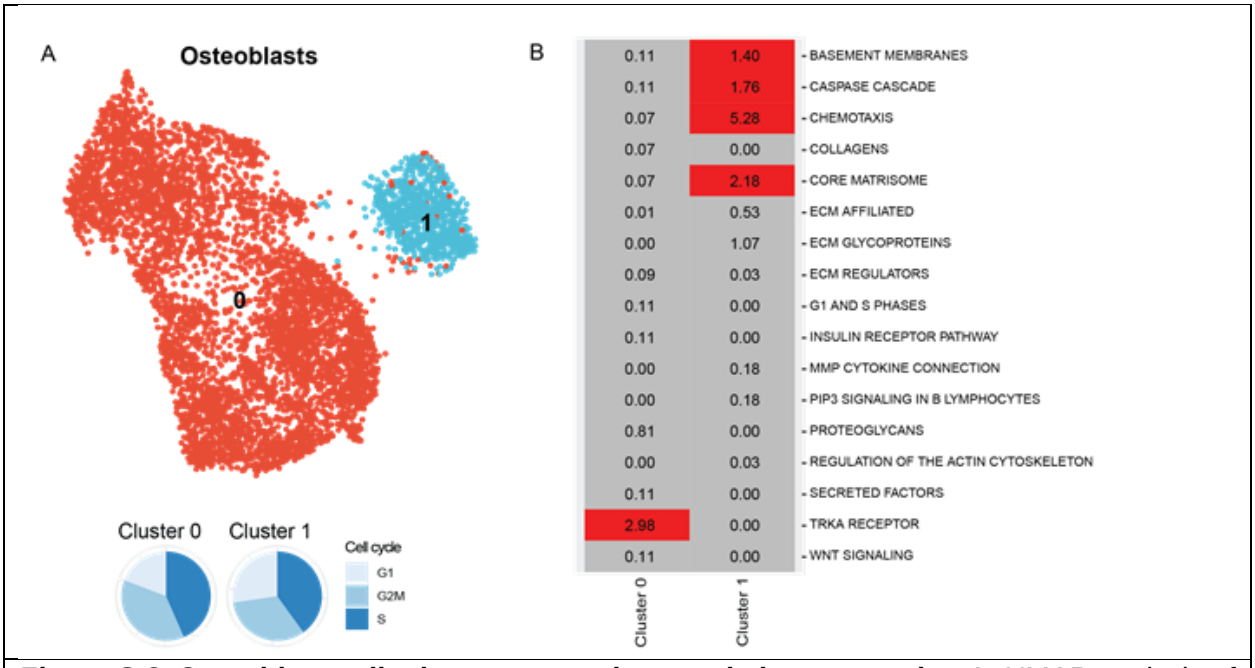

Figure S 2. **Osteoblast cells demonstrate phenotypic heterogeneity.** A. UMAP analysis of normal human osteoblast cells in cell culture B. Pathway enrichment analysis against msigdb C2 canonical pathways on genes differentially upregulated in each cluster relative remaining cells in the dataset.

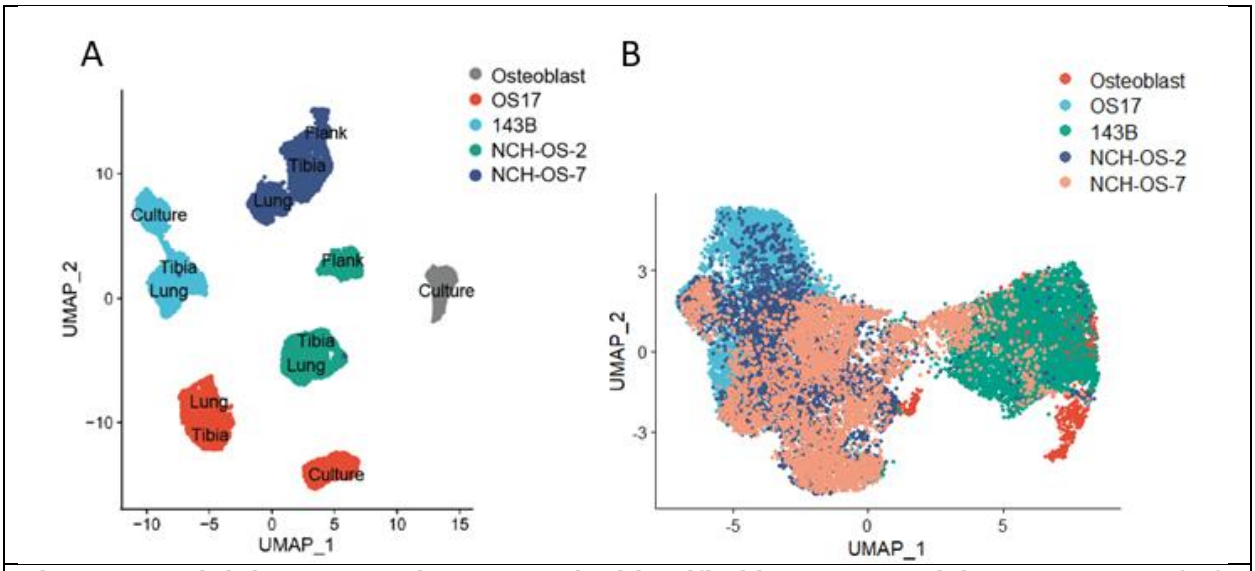

Figure S 3. **High inter-tumor heterogeneity identified between models.** A. UMAP analysis of merged datasets. B. Application of Harmony forces similarity between heterogeneous populations of cells.

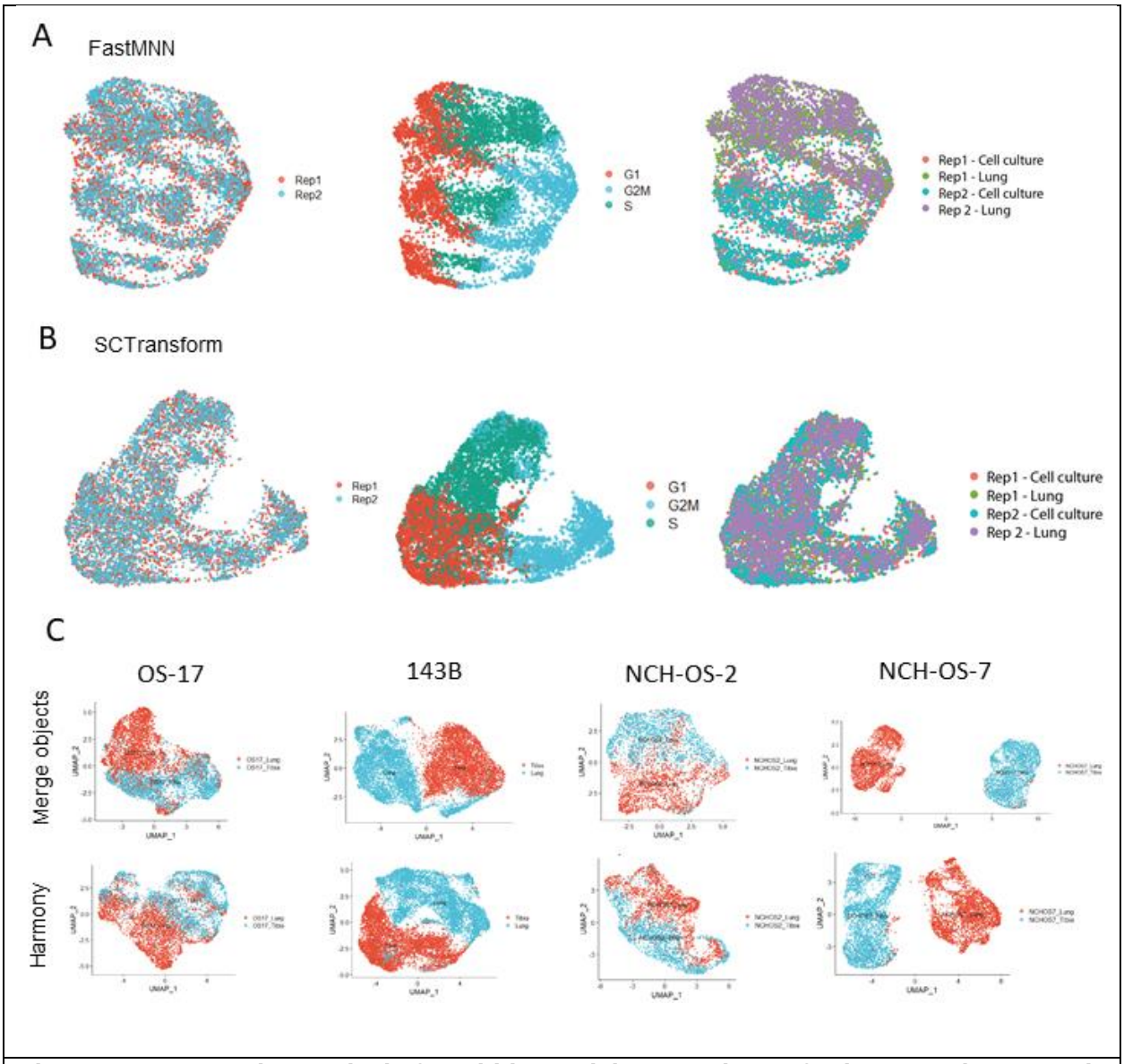

Figure S 4. **Integrative analysis for within-model comparison of primary and metastatic lesions.** A, B Application of FastMNN or SCTransform between replicate samples demonstrated complete overlay, however cells separated largely by state of cell cycle. C. Application of harmony or merging Seurat objects demonstrated similar trend. Cells did not cluster based on state of cell cycle (data not shown).

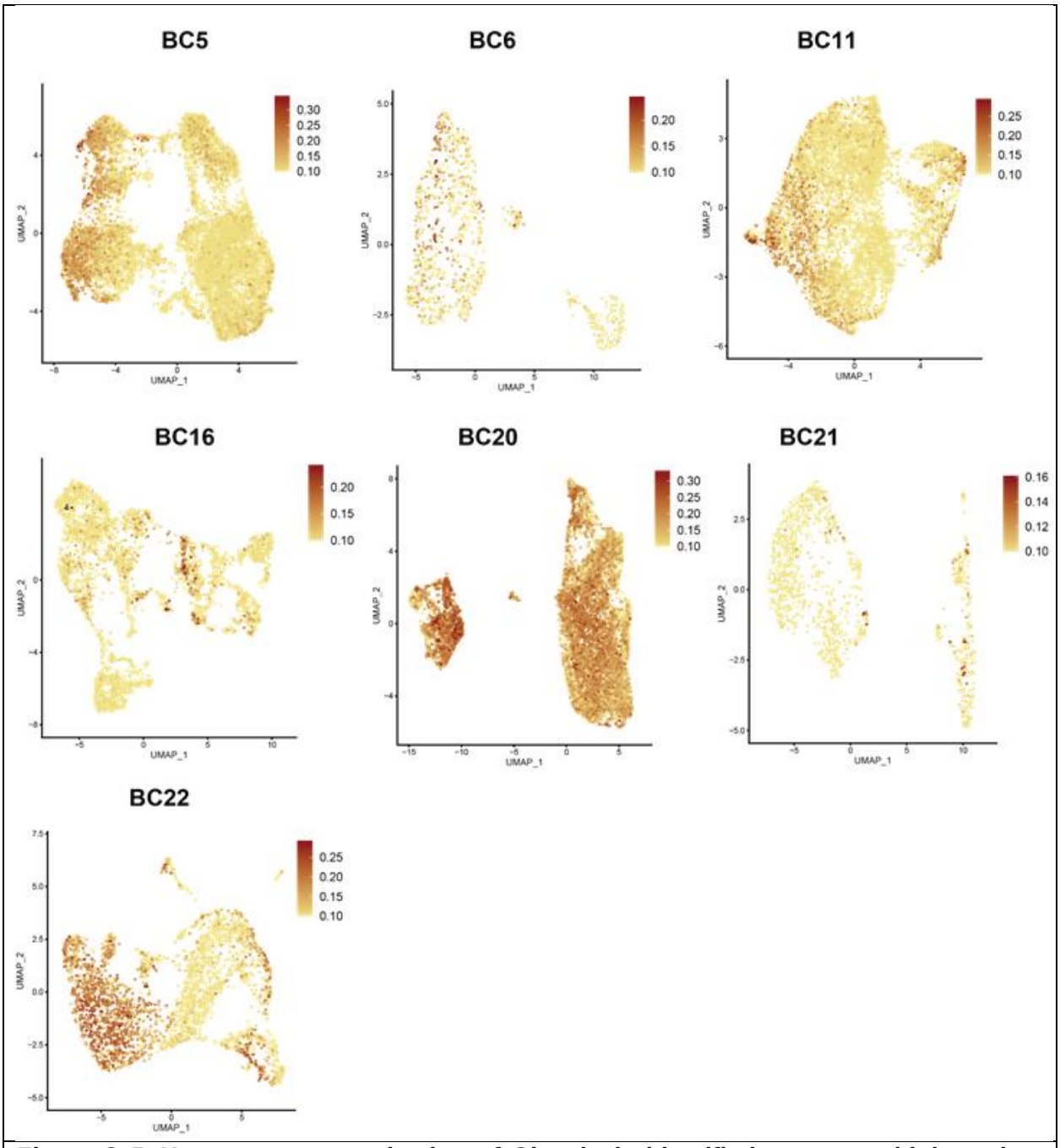

Figure S 5. **Heterogeneous activation of Glycolysis identified across multiple patient primary tumor datasets.** FeaturePlots for Glycolysis module score in each of the datasets. Module score for Glycolysis was calculated using the 'AddModuleScore' function in Seurat with msigdb HALLMARK_GLYCOLYSIS genes as input features for expression program.

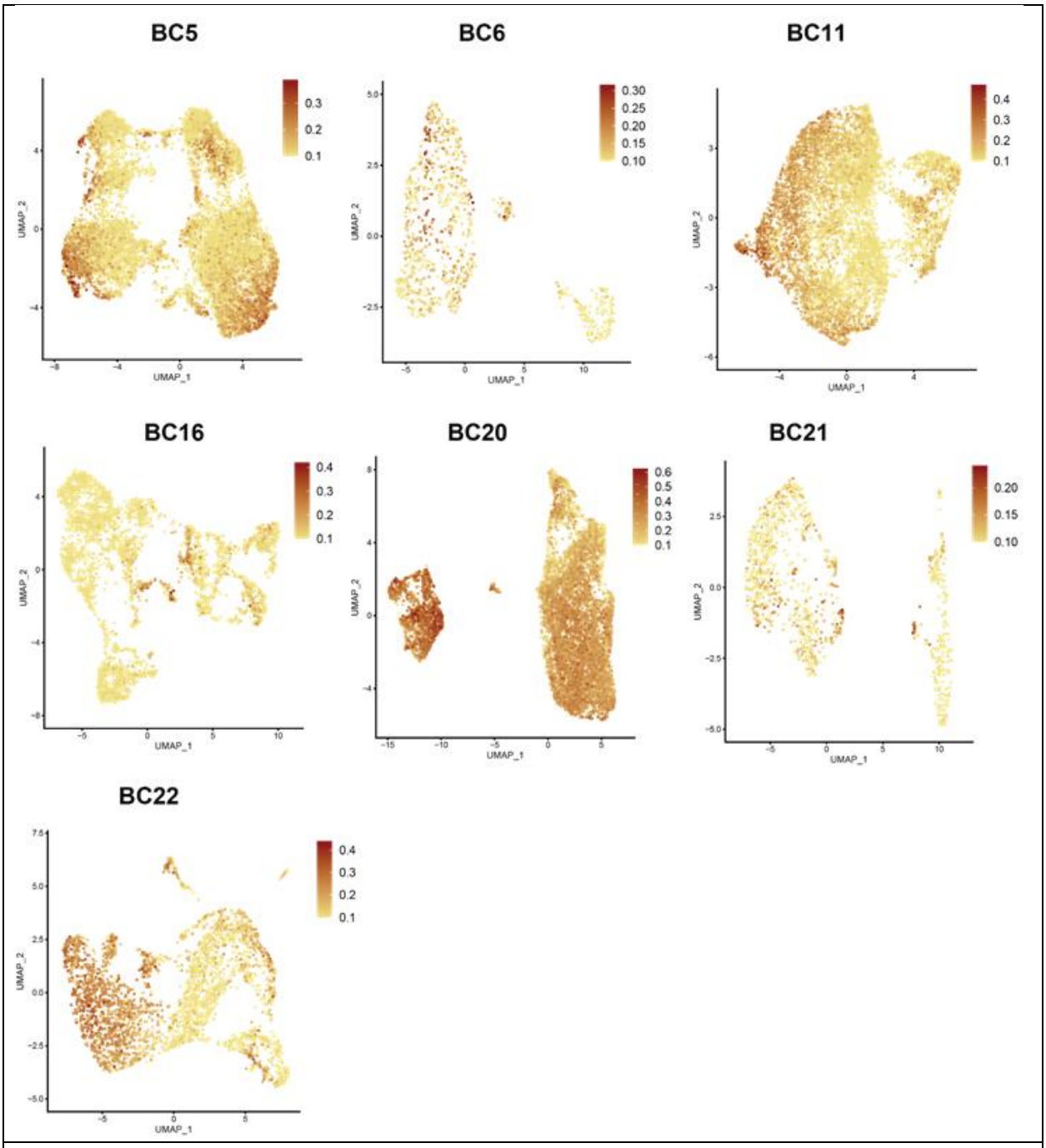

Figure S 6. **Heterogeneous activation of Hypoxia related genes identified across multiple patient primary tumor datasets.** FeaturePlots for Hypoxia module score in each of the datasets. Module score for Hypoxia was calculated using the 'AddModuleScore' function in Seurat with msigdb HALLMARK_HYPOXIA genes as input features for expression program.

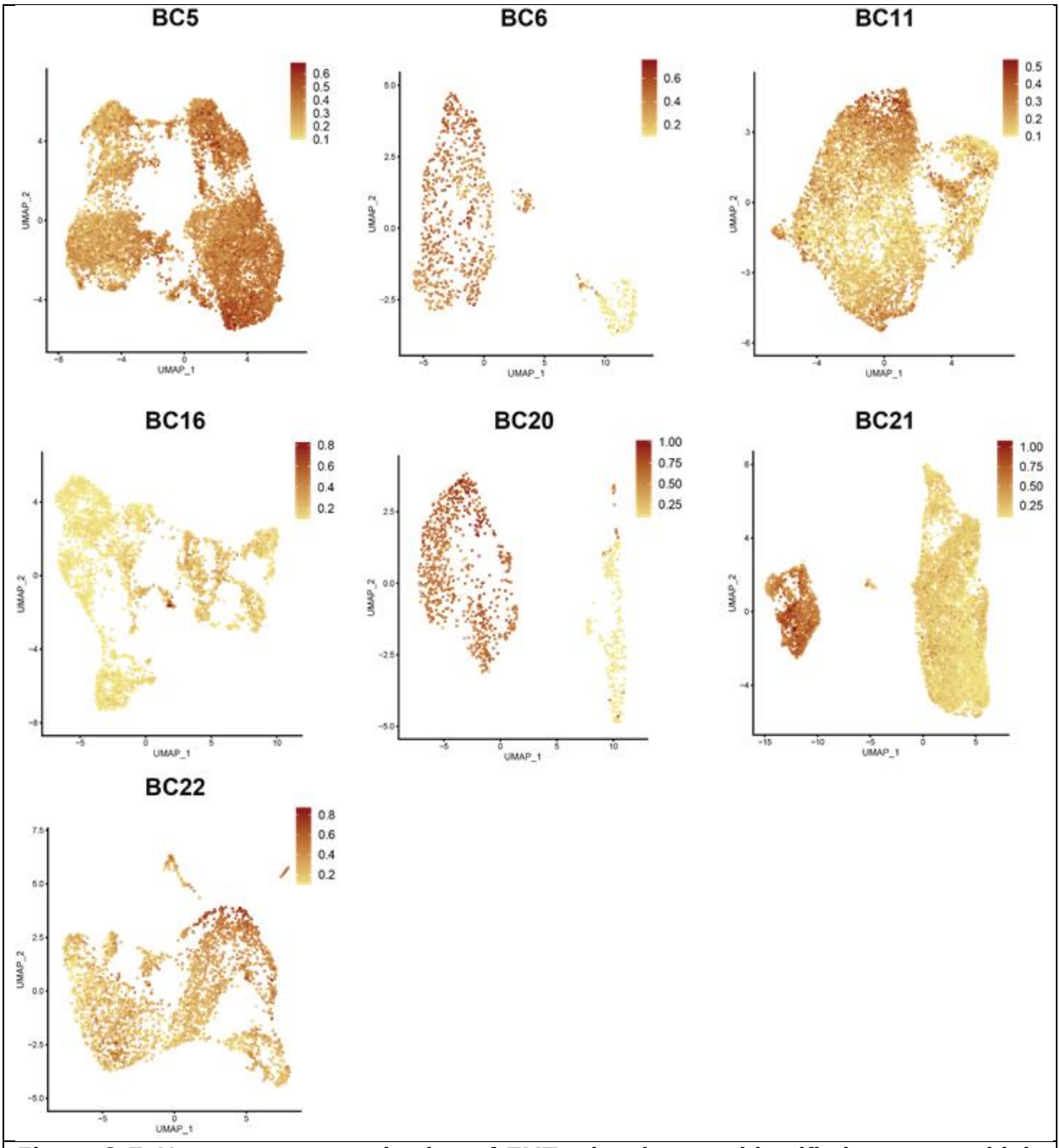

Figure S 7. **Heterogeneous activation of EMT related genes identified across multiple patient primary tumor datasets.** FeaturePlots for EMT module score in each of the datasets. Module score for EMT was calculated using the 'AddModuleScore' function in Seurat with msigdb HALLMARK_EPITHELIAL_MESENCHYMAL_TRANSITION genes as input features for expression program.

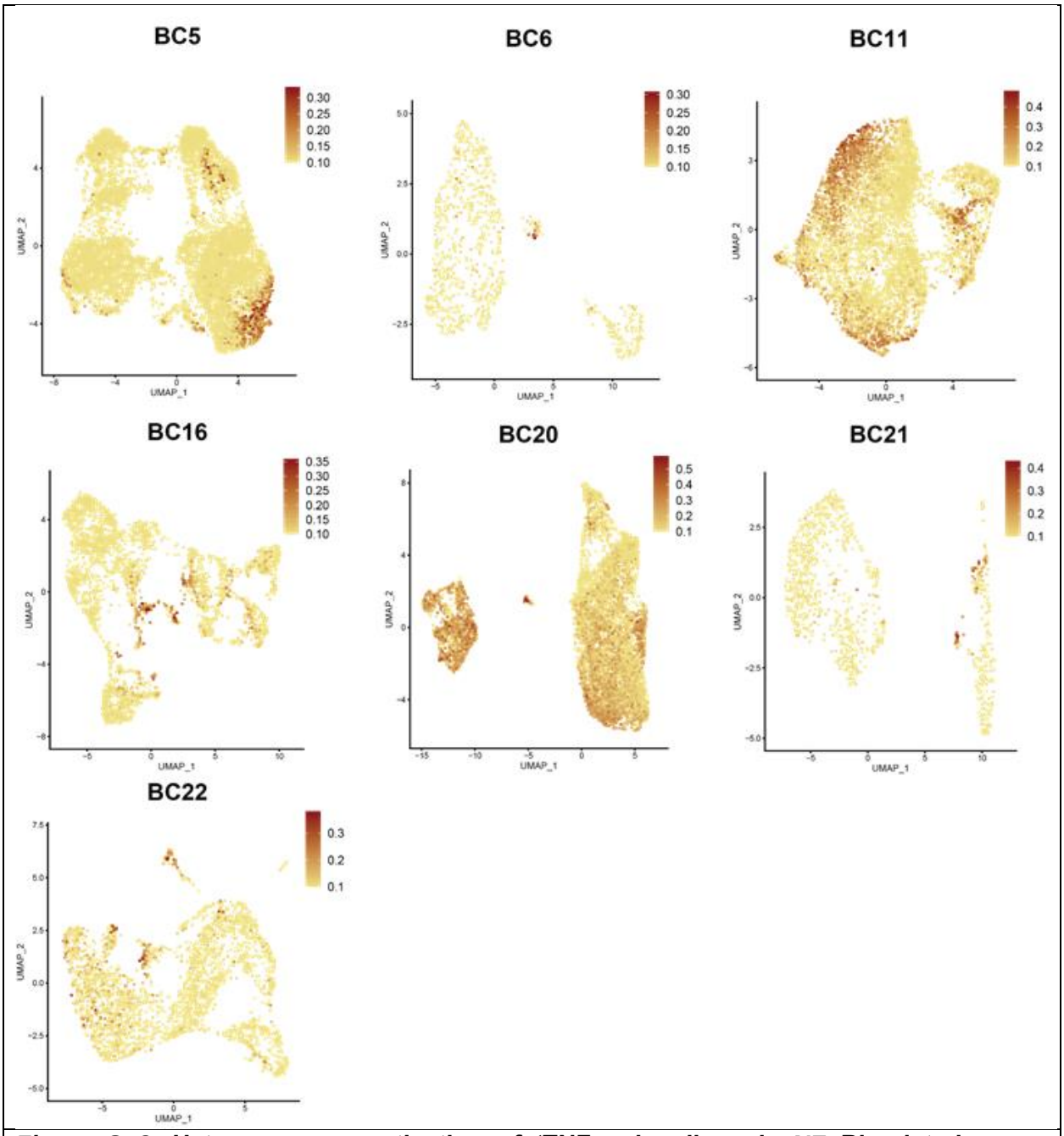

Figure S 8. **Heterogeneous activation of 'TNFα signaling via NFκB' related genes identified across multiple patient primary tumor datasets.** FeaturePlots for TNFα signaling via NFκB module score in each of the datasets. Module score for TNFα signaling via NFκB was calculated using the 'AddModuleScore' function in Seurat with msigdb HALLMARK_TNFα_SIGNALING_VIA_NFκB genes as input features for expression program.

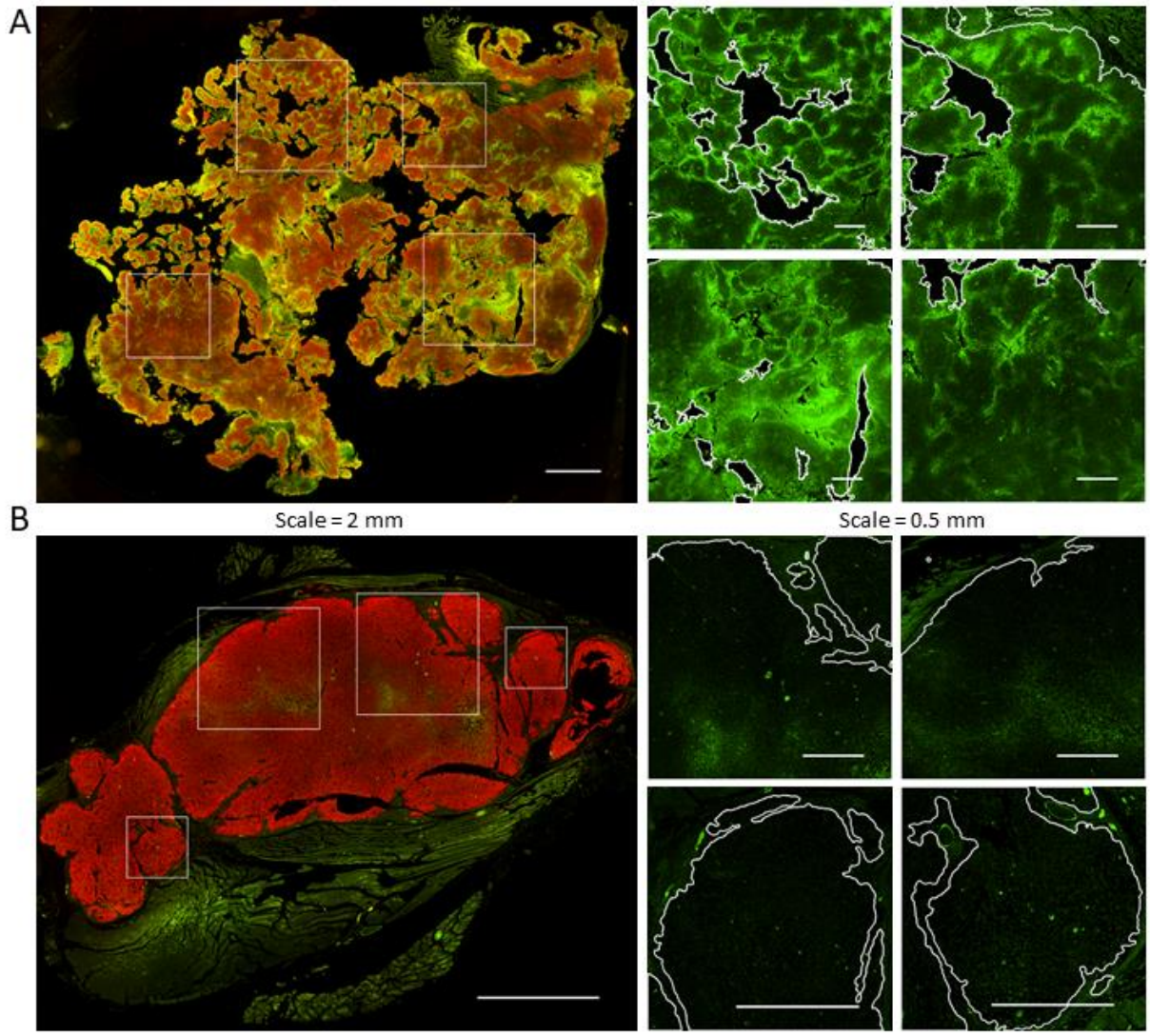

Figure S 9. **Primary tumors demonstrate heterogeneity in GLUT1 staining.** A, B) Immunofluorescence staining of OS-17 and 143B primary tumors, respectively, for GLUT1 (green; a marker of glycolysis) and vimentin (red; marker to identify osteosarcoma cells). Magnified GLUT1 staining is shown for the boxed regions on the whole-section images. Lesion edges are indicated by white outlines in the magnified regions. Tumors showed a high degree of intra-tumor variation in GLUT1 staining intensity.

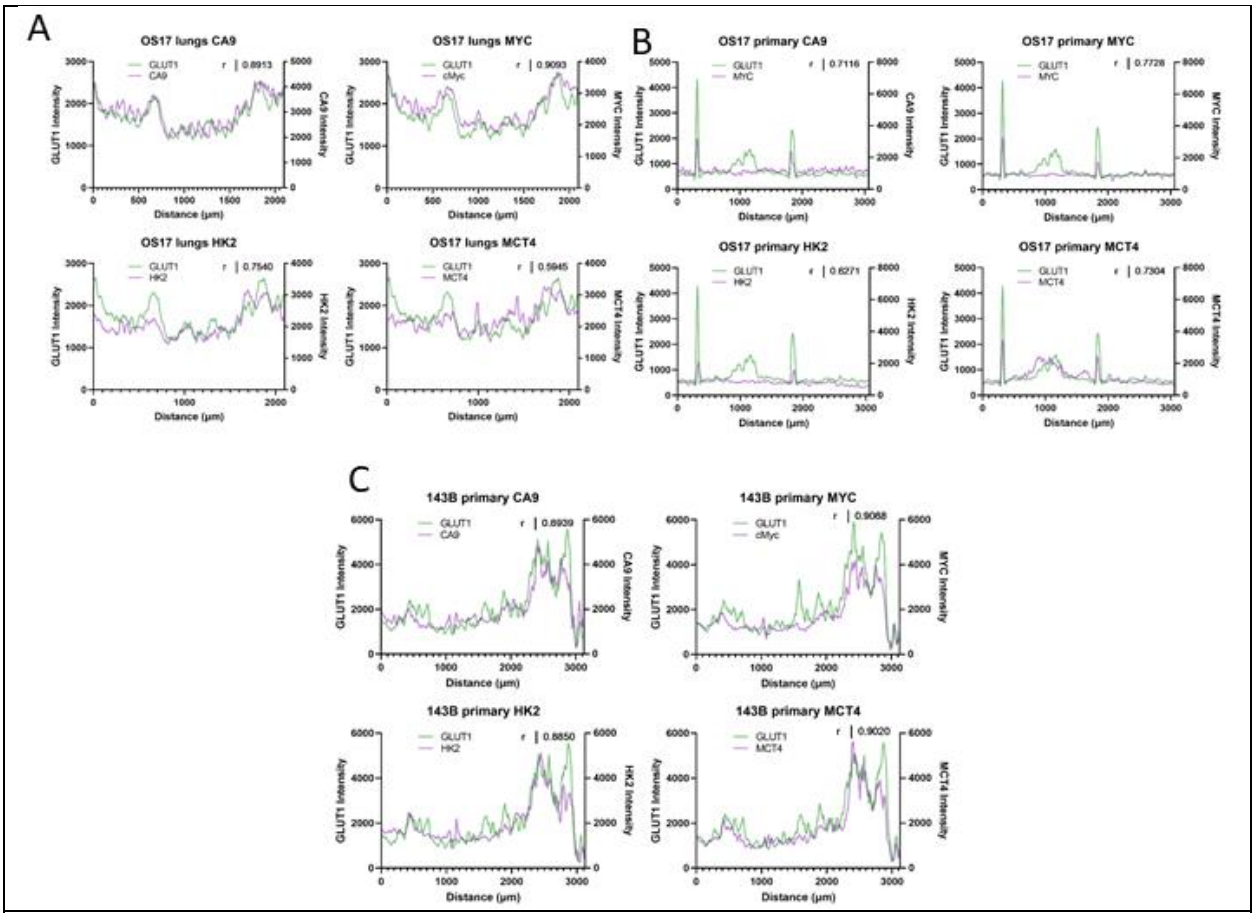

Figure S 10. **High correlation between multiple markers of Glycolysis activation in primary and metastatic osteosarcoma lesions.** Correlation of fluorescence intensity of markers of glycolysis (CA9, HK2, MCT4), an upstream regulator (MYC) with GLUT1 along a ~3mm profile line drawn through the corresponding primary and metastatic lesions. The location and intensity of staining was highly correlated with GLUT1 for all markers.

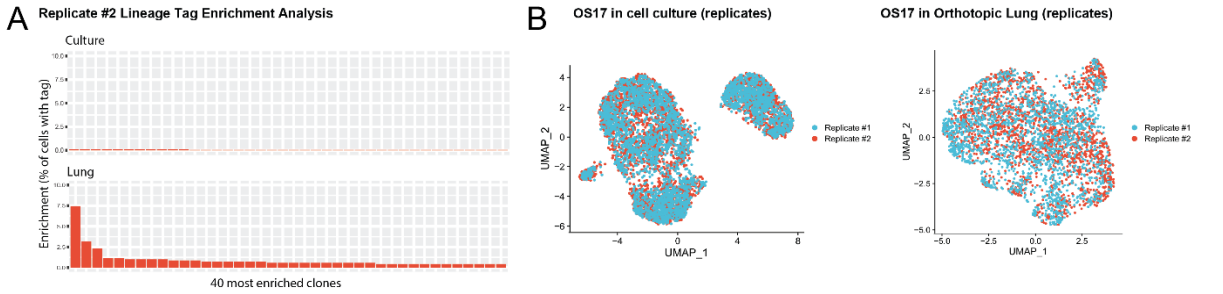

Figure S 11. **Replicates demonstrate reproducible Lineage tag enrichment profiles and consistent phenotypic profiles.** A) Frequency distribution of clones identified in each of the conditions generated using a biological replicate of the starting population (cells infected with separate batch of lentivirus library). B) Admixing of OS-17 cells from distinct, biological replicates grown *in vitro* or as metastatic lesions suggests that intra-tumor transcriptional heterogeneity of osteosarcoma cells is not driven by individual tumor identity.

Table S 1. Characteristics of Patient-Derived Tumor Xenograft Models used in this study

Module	Field	NCH-OS-2	NCH-OS-7
Clinical/patient	Submitter patient ID	X0070	X0140
	Gender	Male	Female
	Age	20-25	15-20
	Diagnosis	Metastatic osteosarcoma	Metastatic osteosarcoma
	Consent to share data	Available to academic centers only	Yes
	Ethnicity/race	Caucasian	Caucasian
	Current treatment drug		
	Virology status	HepA(-), HepB(-), HepC(-), HIV-1(-), HIV-2(-), Mycoplasma(-)	HepA(-), HepB(-), HepC(-), HIV-1(-), HIV-2(-), Mycoplasma(-)
Clinical/tumor	Submitter tumor ID	X0070	X0140
	Primary tumor tissue of origin	Bone	Bone
	Primary, metastasis, recurrence	Metastasis	Recurrence
	Specimen tumor tissue	Lung	Lung
	Tumor grade; classification	High Grade	High grade
	Disease stage; classification	metastatic osteosarcoma	metastatic osteosarcoma
	Specific markers (diagnostic linked); platform	N/A	N/A
	Is tumor from untreated patient?	Yes	No
	Original tumor sample type	Surgical resection	Open biopsy
	Tumor from an existing PDX model? ID? Why sub-line?	No	No
Model creation	Submitter PDX ID	NCH-OS-2	NCH-OS-7

	Mouse strain (and source)	C.B-17/IcrHan Hsd-Prkdcscid	C.B-17/IcrHan Hsd-Prkdcscid
	Strain immune system humanized?	No	No
	Type of humanization	NA	NA
	Tumor preparation	Solid tumor fragments and cell suspension	Solid tumor fragments and cell suspension
	Injection type and site	Subcutaneous, flank; Intravenous, tail vien; Intraosseous, tibial plate	Subcutaneous, flank; Intravenous, tail vien; Intraosseous, tibial plate
Model quality assurance	Tumor characterization technology	Histology and IHC	Histology and IHC
	Tumor confirmed not to be of mouse/EBV origin	84% Human tissue	76% Human tissue
	Passage QA performed	Passage P3	Passage P5
Model study	Treatment, passage	No previous treatment	No previous treatment
Associated metadata	PDX model availability?	Yes, frozen tumor	Yes, frozen tumor
	Governance restriction for distribution	Available to academic centers only	Available to academic centers only

Table S 2. Relative percentage of cells distributed between clusters in each model between Tibia and Lung colonization conditions

OS-17	Condition	Cluster	Relative percentage
	Tibia	0	50.26325
	Tibia	1	43.45384
	Tibia	2	1.053001
	Tibia	3	5.229905
	Lung	0	46.57775
	Lung	1	10.17901
	Lung	2	39.69814
	Lung	3	3.545104

143B	Tibia	0	97.89638
	Tibia	1	1.149201
	Tibia	2	0.447994
	Tibia	3	0.506428
	Lung	0	2.220491
	Lung	1	92.30619
	Lung	2	3.350214
	Lung	3	2.123101
NCH-OS-2	Tibia	0	82.28155
	Tibia	1	5.339806
	Tibia	2	12.37864
	Lung	0	20.32767
	Lung	1	71.48058
	Lung	2	8.191748
NCH-OS-2	Tibia	0	0
	Tibia	1	59.4258
	Tibia	2	40.5742
	Tibia	3	0
	Lung	0	71.01349
	Lung	1	1.383604
	Lung	2	1.176064
	Lung	3	26.42684

Table S 3. Table showing differentially upregulated genes in the top ten enriched clonal families relative to the remaining metastatic OS-17 cells

	P value	Average log2(fold-change)	Adjusted p value
PTPRZ1	3.49E-24	0.340175	7.04E-20
CD9	9.46E-21	0.522326	1.91E-16
GZMB	3.52E-20	0.360582	7.1E-16
ENO2	8.76E-16	0.516978	1.77E-11
AQP1	1.84E-15	0.298789	3.71E-11
CDC42EP3	2.58E-14	0.302923	5.2E-10
P4HA2	1.1E-12	0.515958	2.21E-08
TGFBI	1.57E-12	0.522179	3.16E-08
COL6A2	3.66E-12	0.456208	7.37E-08

BEX1	9.34E-12	0.252685	1.88E-07
WDR54	1.21E-11	0.264337	2.44E-07
S100A10	6.43E-11	0.308953	1.3E-06
MIF	7.32E-10	0.370393	1.47E-05
TPI1	4.65E-09	0.285224	9.38E-05
ENO1	6.68E-09	0.468255	0.000135
VEGFA	2.77E-08	0.752467	0.000558
FLNB	2.92E-08	0.260708	0.000589
COL6A1	1.18E-07	0.287235	0.002379
PGK1	2.51E-07	0.609942	0.005059
S100A2	3.03E-07	0.421746	0.006097
GBE1	3.05E-07	0.318568	0.006149
SEC61G	4.59E-07	0.258519	0.009259
PFKP	5.71E-07	0.331277	0.011517
FAM162A	5.76E-07	0.682216	0.011619
BEND5	6.43E-07	0.251597	0.012955
LGALS3	1.98E-06	0.342243	0.997

Table S 4. Lineage tag distribution statistics for two biological replicates

Replicate 1		
Number of copies	Frequency	Percentage
1	2283	69.4
2	659	20.0
3	217	6.6
4	76	2.3
5	32	1.0
6	10	0.3
7	9	0.3
11	1	0.0
13	1	0.0
14	1	0.0
Replicate 2		
Number of copies	Frequency	Percentage
1	482	84.0

2	69	12.0
3	15	2.6
4	6	1.0
5	2	0.3

Table S 5. Lineage tag summary statistics for two biological replicates

Replicate 1	
Summary Statistics	
Min.	1
1stQu.	1
Median	1
Mean	1.483
3rdQu.	2
Max.	14
Replicate 2	
Summary Statistics	
Min.	1
1stQu.	1
Median	1
Mean	1.218
3rdQu.	1
Max.	5